JOURNAL OF GEOPHYSICAL RESEARCH, VOL. 112, B09301, doi:10.1029/2007JB004944, 2007

Influence of fore-arc structure on the extent of great subduction zone earthquakes

Andrea L. Llenos[1] and Jeffrey J. McGuire[2]

Received 19 January 2007; revised 3 May 2007; accepted 13 June 2007; published 6 September 2007.

[1] Structural features associated with fore-arc basins appear to strongly influence the rupture processes of large subduction zone earthquakes. Recent studies demonstrated that a significant percentage of the global seismic moment release on subduction zone thrust faults is concentrated beneath the gravity lows resulting from fore-arc basins. To better determine the nature of this correlation and to examine its effect on rupture directivity and termination, we estimated the rupture areas of a set of M_w 7.5–8.7 earthquakes that occurred in circum-Pacific subduction zones. We compare synthetic and observed seismograms by measuring frequency-dependent amplitude and arrival time differences of the first orbit Rayleigh waves. At low frequencies, the amplitude anomalies primarily result from the spatial and temporal extent of the rupture. We then invert the amplitude and arrival time measurements to estimate the second moments of the slip distribution which describe the rupture length, width, duration, and propagation velocity of each earthquake. Comparing the rupture areas to the trench-parallel gravity anomaly (TPGA) above each rupture, we find that in 11 of the 15 events considered in this study the TPGA increases between the centroid and the limits of the rupture. Thus local increases in TPGA appear to be related to the physical conditions along the plate interface that favor rupture termination. Owing to the inherently long timescales required for fore-arc basin formation, the correlation between the TPGA field and rupture termination regions indicates that long-lived material heterogeneity rather than short timescale stress heterogeneities are responsible for arresting most great subduction zone ruptures.

Citation: Llenos, A. L., and J. J. McGuire (2007), Influence of fore-arc structure on the extent of great subduction zone earthquakes, *J. Geophys. Res.*, *112*, B09301, doi:10.1029/2007JB004944.

1. Introduction

[2] The largest earthquakes in the world occur in subduction zones, where almost 90% of the total global seismic moment is released [*Lay and Bilek*, 2007]. However, the amount of seismic coupling widely varies from one subduction zone to another, ranging from predominantly aseismic subduction in the Marianas to seismic subduction in Alaska [e.g., *Scholz and Campos*, 1995; *Lay and Bilek*, 2007]. Understanding this variation in earthquake occurrence in circum-Pacific subduction zones has been the subject of numerous studies. The correlations between earthquake occurrence and such factors as age of subducting oceanic lithosphere, amount of sediment, bathymetric features on the subducting slab, and convergence rate have been investigated [e.g., *Mogi*, 1969; *Kelleher and McCann*, 1976; *Ruff and Kanamori*, 1980; *Pacheco et al.*, 1993; *Scholz and Campos*, 1995; *Abercrombie et al.*, 2001]. However, wide variability in seismogenic behavior exists not only between different subduction zones but within individual subduction zones themselves.

[3] The asperity model is commonly used to describe this variability in seismic behavior [*Lay and Kanamori*, 1981]. The moment release during great earthquakes is nonuniform, and the areas of high moment release are known as asperities. These asperities may occur because of variability in frictional properties on the plate interface, which may lock during the interseismic period and suddenly release slip in an earthquake [e.g., *Lay et al.*, 1982]. An alternative view is that time-dependent stress heterogeneity is the dominant factor controlling the extent of great earthquakes. Numerical simulations demonstrated that even a fault with uniform frictional properties can generate a complex sequence of events that rupture different portions of the fault in each rupture rather than repeatedly at a fixed asperity [*Shaw*, 2000]. In this model, large earthquakes preferentially nucleate at the edge of a previous large rupture and propagate in the opposite direction providing a natural explanation for the observation that large subduction zone ruptures are predominantly unilateral along strike [*McGuire et al.*, 2002]. Moreover, *Thatcher* [1989] used historical estimates of rupture area for great subduction zone earthquakes to argue that these events are rarely repeats of the previous big earthquake and instead fill in regions where stress accumulation has not been relieved recently (the

[1]MIT/WHOI Joint Program, Cambridge, Massachusetts, USA.
[2]Department of Geology and Geophysics, Woods Hole Oceanographic Institution, Woods Hole, Massachusetts, USA.

0148-0227/07/2007JB004944$09.00

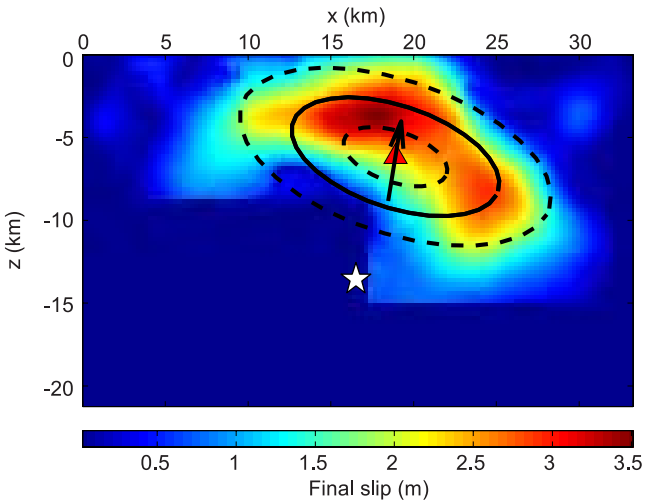

Figure 1. Characteristic rupture ellipse for the 2000 Tottori earthquake (solid black line), rupture directivity (arrow), centroid location (triangle), and hypocenter location (star) plotted on top of slip model of *Iwata et al.* [2000].

seismic gap hypothesis). While both ''quenched heterogeneity'' (the asperity model) and ''dynamic heterogeneity'' (the seismic gap hypothesis) likely influence the details of individual ruptures to some extent, it is very important to determine which is the dominant behavior in subduction zones as they have very different implications for the long-term seismic hazard at a particular location.

[4] In a given subduction zone, the trench-normal controls on earthquake rupture are relatively well understood. The fault width is constrained by the updip and downdip limits of the seismogenic zone, at depths of 5–10 km and 25–55 km, respectively [e.g., *Byrne et al.*, 1988; *Pacheco et al.*, 1993; *Tichelaar and Ruff*, 1993; *Oleskevich et al.*, 1999; *Lay and Bilek*, 2007]. These limits result from transitions from velocity-strengthening to velocity-weakening behavior [*Scholz*, 2002]. These transitions likely occur because of changes in properties such as sediment strength and mineral composition due to changing pressure and temperature conditions [e.g., *Byrne et al.*, 1988; *Hyndman and Wang*, 1993; *Oleskevich et al.*, 1999].

[5] However, subduction zone earthquakes can release large amounts of seismic moment because extremely long fault lengths are possible along a subduction zone. An important question then becomes: what controls the along-strike limits of these great earthquakes? What stops a M_w 7.0 earthquake from continuing to rupture along a subduction zone and becoming a M_w 9.0 earthquake? Some studies have shown that transverse structures such as ridges or seamounts in the subducting lithosphere often fragment the subduction zone and may provide natural barriers to rupture [e.g., *Mogi*, 1969; *Kelleher and McCann*, 1976; *Cloos*, 1992; *Kodaira et al.*, 2000, 2002]. However, such structures can also prove to be asperities, as *Abercrombie et al.* [2001] found in the case of the 1994 Java tsunamigenic earthquake, where the majority of the seismic moment release was centered on a subducted seamount. Therefore the relationship between subducting geological structure and the extent of large individual ruptures remains unclear.

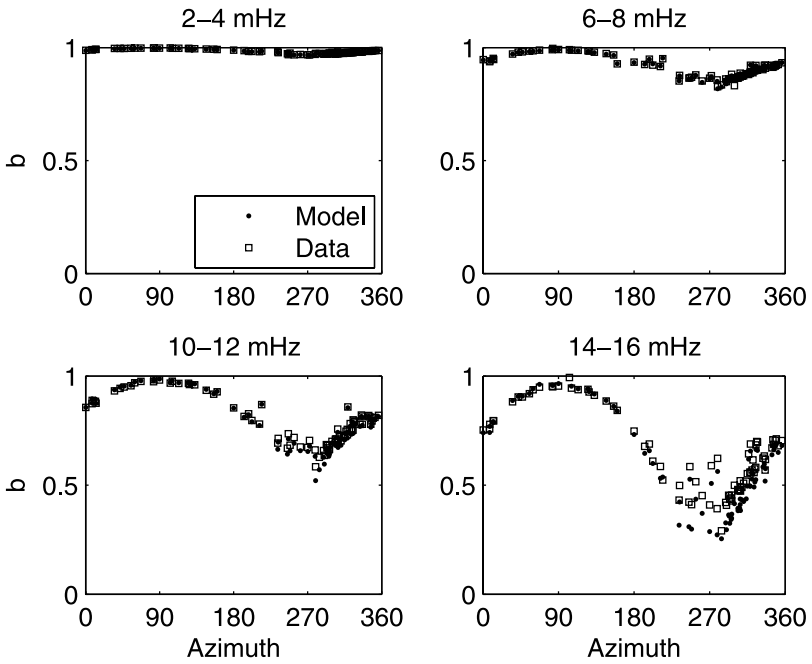

Figure 2. Amplitude measurements (square) and model (circle) from a synthetic line source test at different frequency bands. The 3-D point source synthetics were used to simulate a 70 km long unilateral rupture propagating to the east with a velocity of 2.5 km/s. Low-amplitude measurements at azimuths of 270 confirm that rupture propagated away from the west. The amplitude anomaly increases with frequency. In general, the model fits the measurements well at lower frequencies, but at the 14–16 mHz band they begin to differ significantly.

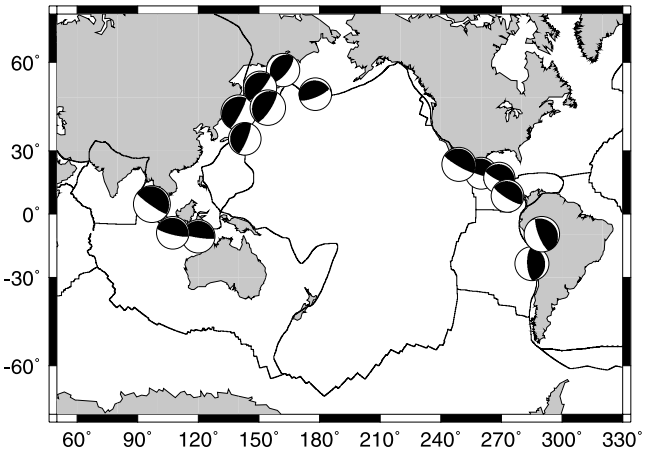

Figure 3. Location and focal mechanisms of the 15 M_w > 7.5 events in data set.

[6] The upper plate also plays an important role in earthquake rupture. *McCaffrey* [1993] emphasized the importance of fore-arc rheology in seismogenic behavior; strong fore arcs produce more large earthquakes because of their ability to store elastic strain energy. Recent studies by *Song and Simons* [2003] and *Wells et al.* [2003] have demonstrated that large subduction zone earthquakes occur preferentially in areas along the plate interface which are overlain by fore-arc basins. *Song and Simons* [2003] found that 80% of the cumulative seismic moment release in the 20th century occurred in the 30% of the total area of subduction zone which exhibited strongly negative gravity anomalies, indicators of the presence of fore-arc basins. Fore-arc basins tend to form in strong, stable wedges and therefore reflect the mechanical and frictional properties along the plate interface over which they lay [*Byrne et al.*, 1988; *Fuller et al.*, 2006; *Wang and Hu*, 2006]. To what extent then can fore-arc structure influence the rupture of individual earthquakes?

[7] This study aims to investigate the relationship between earthquake rupture propagation and fore-arc structure in greater detail. Where do large events start and stop with respect to along-strike structures in the gravity field? To address this question, we estimated the finite source properties of a set of 15 subduction zone thrust events (M_w > 7.5) and compared them to fore-arc structure revealed by maps of trench-parallel gravity anomalies (TPGA) constructed by *Song and Simons* [2003]. We find that as a rupture approaches its eventual extent, the TPGA increases. This correlation, which reinforces the observations of *Song and Simons* [2003], suggests that the stress and frictional heterogeneities along the plate interface that control the rupture of large subduction zone earthquakes are expressed in the fore-arc gravity field.

2. Methodology

[8] To evaluate the relationships between fore-arc structure and individual ruptures, we require well constrained information on the spatial extent of rupture that can be determined in subduction zones worldwide. This is often a difficult observational problem because most subduction zone ruptures occur offshore and often with limited geodetic and near-field seismic data. Even for the best data sets, detailed finite fault inversions of great subduction zone earthquakes are highly sensitive to model parameterization and station coverage. An example of this is the 2003 M_w 8.3 Tokachi-oki earthquake. Despite the abundance of quality seismic and geodetic data recorded during the event, by far the best data set ever for a M_w 8 subduction zone rupture, the finite fault models produced following the earthquake differ in characteristics such as number of asperities and orientation of rupture [*Miyazaki et al.*, 2004a]. Some studies found that the rupture was oriented more along strike of the trench [*Yamanaka and Kikuchi*, 2003] while others found rupture areas that were half the size and oriented downdip [*Yagi*, 2004; *Honda et al.*, 2004; *Koketsu et al.*, 2004; *Miyazaki et al.*, 2004a]. The differences between the slip models highlight the sensitivity of the results to the different fault parameterizations, constraints, and data sets used in each study. Even for the best combined seismic and geodetic data sets, the rupture area is only constrained to within a factor of two owing to the limited offshore coverage. Moreover, body wave based studies often have poor constraints on the seismic moment and slip distribution owing to their relatively high frequency band [*Pritchard et al.*, 2007].

[9] An alternative approach is to utilize seismic surface waves to constrain only the gross features of the rupture,

Table 1. Characteristic Rupture Dimensions of the Events in This Study[a]

Event	Location	M_w	L_c, km	τ_c, s	$\lvert\boldsymbol{v_0}\rvert$, km/s	Directivity Ratio
19920902	Nicaragua	7.6	74 ± 7	40 ± 1	1.8 ± 0.1	0.97 ± 0.10
19940602	Java, Indonesia	7.8	86 ± 7	16 ± 2	4.2 ± 1.3	0.78 ± 0.19
19941228	Sanriku-oki, Honshu, Japan	7.7	161 ± 14	20 ± 3	6.1 ± 1.9	0.77 ± 0.16
19950730	Antofagasta, Chile	8.0	121 ± 10	33 ± 1	1.3 ± 0.1	0.35 ± 0.04
19950914	Copala, Mexico	7.3	74 ± 4	14 ± 1	3.2 ± 0.3	0.62 ± 0.06
19951009	Jalisco, Mexico	8.0	77 ± 6	32 ± 1	2.1 ± 0.1	0.86 ± 0.08
19951203	Kurile Islands, Russia	7.9	121 ± 9	36 ± 1	1.1 ± 0.1	0.32 ± 0.03
19971205	Kamchatka, Russia	7.8	58 ± 2	34 ± 1	1.6 ± 0.1	0.95 ± 0.02
20010623	Arequipa, Peru	8.4	167 ± 2	27 ± 1	1.1 ± 0.2	0.18 ± 0.02
20030122	Colima, Mexico	7.5	92 ± 6	29 ± 1	1.4 ± 0.1	0.44 ± 0.03
20030925	Tokachi-oki, Hokkaido, Japan	8.3	40 ± 2	45 ± 1	0.9 ± 0.1	0.96 ± 0.02
20031117	Rat Islands, Alaska	7.8	70 ± 21	29 ± 1	2.2 ± 0.4	0.91 ± 0.24
20050328	Sumatra, Indonesia	8.7	137 ± 19	47 ± 3	2.3 ± 0.3	0.79 ± 0.15
20060717	Java, Indonesia	7.7	108 ± 5	55 ± 1	1.9 ± 0.1	0.98 ± 0.05
20061115	Kurile Islands, Russia	8.3	93 ± 3	52 ± 1	1.8 ± 0.1	0.98 ± 0.02

[a]Event number is date as year, month, day. Errors are ±1 standard deviation.

Table 2. Second Moments Inversion Results[a]

		$\hat{\boldsymbol{\mu}}^{(1,1)}$			$\hat{\boldsymbol{\mu}}^{(2,0)}$					
Earthquake	$\hat{\mu}^{(0,2)}$	r	θ	φ	rr	rθ	rφ	$\theta\theta$	$\theta\varphi$	$\varphi\varphi$
Nicaragua	406 ± 23	−11 ± 3	374 ± 19	615 ± 14	6 ± 1	−10 ± 6	−18 ± 7	423 ± 225	586 ± 131	997 ± 135
Java	65 ± 19	26 ± 4	−70 ± 20	262 ± 19	56 ± 1	214 ± 46	60 ± 17	1514 ± 291	−467 ± 132	1140 ± 170
Sanriku-oki	103 ± 29	4 ± 2	−292 ± 14	−555 ± 18	0.3 ± 0.3	−4 ± 3	−26 ± 9	1093 ± 231	990 ± 127	6260 ± 1089
Antofagasta	280 ± 24	22 ± 2	351 ± 14	−53 ± 17	4.7 ± 0.4	48 ± 5	−26 ± 3	1983 ± 272	−1682 ± 271	1963 ± 381
Copala	51 ± 5	−10 ± 1	−145 ± 4	79 ± 4	3.1 ± 0.4	18 ± 4	−44 ± 5	601 ± 63	237 ± 43	1311 ± 126
Jalisco	259 ± 10	12 ± 3	−379 ± 14	−373 ± 11	8 ± 1	−15 ± 10	−18 ± 9	842 ± 135	686 ± 107	730 ± 109
Kurile	320 ± 18	−28 ± 4	−306 ± 13	164 ± 16	4 ± 1	29 ± 2	−46 ± 5	433 ± 124	−434 ± 85	3607 ± 563
Kamchatka	289 ± 6	−41 ± 2	310 ± 17	−345 ± 16	91 ± 13	9 ± 8	93 ± 8	459 ± 42	−363 ± 31	486 ± 42
Arequipa	187 ± 16	45 ± 5	81 ± 11	187 ± 22	206 ± 2	329 ± 16	192 ± 45	739 ± 14	−737 ± 28	6859 ± 177
Colima	210 ± 8	0 ± 4	−264 ± 12	129 ± 8	2.0 ± 0.4	−7 ± 5	−6 ± 3	1726 ± 229	717 ± 119	725 ± 102
Tokachi-oki	500 ± 10	−2 ± 3	−434 ± 20	−44 ± 8	0.4 ± 0.2	2 ± 2	−0.4 ± 0.3	406 ± 30	26 ± 12	178 ± 32
Rat Islands	208 ± 18	−6 ± 3	−59 ± 9	−459 ± 55	0.8 ± 0.1	1 ± 3	12 ± 3	151 ± 208	−15 ± 305	1228 ± 725
Sumatra	559 ± 73	15 ± 5	1200 ± 42	416 ± 35	2 ± 1	31 ± 11	14 ± 5	4503 ± 1031	−660 ± 581	2117 ± 854
Java	761 ± 31	49 ± 5	1022 ± 22	1053 ± 24	5 ± 1	65 ± 5	68 ± 7	1435 ± 112	1402 ± 61	1613 ± 321
Kurile	667 ± 12	−50 ± 5	−1077 ± 38	472 ± 20	41 ± 1	71 ± 7	−31 ± 3	1804 ± 106	−788 ± 50	431 ± 26

[a]Errors are ±1 standard deviation. Units of $\hat{\mu}^{(0,2)}$ are s^2, units of $\hat{\boldsymbol{\mu}}^{(1,1)}$ are km s, and units of $\hat{\boldsymbol{\mu}}^{(2,0)}$ are km^2.

such as its extent and directivity. Surface waves have the natural advantages of complete azimuthal coverage and of being inherently low-frequency such that they are sensitive to the entire moment release even for M_w 8.5 ruptures. Moreover, properties such as directivity and rupture extent can be estimated independent of any smoothing constraints or other a priori information [*McGuire et al.*, 2001]. We quantify the extent and directivity of large ruptures using the second moments of a scalar source-space-time function describing the moment release distribution [*Backus and Mulcahy*, 1976a, 1976b; *Backus*, 1977a, 1977b; *McGuire et al.*, 2001]. The second moments describe the length, width and duration of the area of greatest seismic moment release during an earthquake. They are defined as

$$\hat{\boldsymbol{\mu}}^{(2,0)} = \int\int \dot{f}(\mathbf{r},t)(\mathbf{r}-\mathbf{r_0})(\mathbf{r}-\mathbf{r_0})^T dVdt \tag{1}$$

$$\hat{\mu}^{(0,2)} = \int\int \dot{f}(\mathbf{r},t)(t-t_0)^2 dVdt \tag{2}$$

$$\hat{\boldsymbol{\mu}}^{(1,1)} = \int\int \dot{f}(\mathbf{r},t)(\mathbf{r}-\mathbf{r_0})(t-t_0) dVdt \tag{3}$$

where $\dot{f}$ is the source-space-time function and is proportional to slip rate at a point on the fault, $\mathbf{r_0}$ and t_0 are the centroid location and time, $\hat{\boldsymbol{\mu}}^{(2,0)}$ is the second spatial moment, $\hat{\mu}^{(0,2)}$ is the second temporal moment, and $\hat{\boldsymbol{\mu}}^{(1,1)}$ is the mixed moment which describes overall rupture directivity [*McGuire et al.*, 2001].

[10] The second moments represent weighted averages of seismic moment release, and they define characteristic rupture dimensions that are somewhat smaller than the total rupture dimensions. These characteristic rupture dimensions are [*Silver*, 1983; *Silver and Jordan*, 1983; *McGuire et al.*, 2001]

$$x_c(\hat{\mathbf{n}}) = 2\sqrt{\hat{\mathbf{n}}^T(\hat{\boldsymbol{\mu}}^{(2,0)}/M_0)\hat{\mathbf{n}}} \tag{4}$$

$$\tau_c = 2\sqrt{\hat{\mu}^{(0,2)}/M_0} \tag{5}$$

$$v_c = L_c/\tau_c \tag{6}$$

$$\mathbf{v_0} = \hat{\boldsymbol{\mu}}^{(1,1)}/\hat{\mu}^{(0,2)} \tag{7}$$

where M_0 is the seismic moment and $x_c(\hat{\mathbf{n}})$ is the characteristic dimension of slip in the direction of $\hat{\mathbf{n}}$, which has its maximum value of L_c when $\hat{\mathbf{n}}$ corresponds to the largest eigenvector associated with the largest eigenvalue of $\hat{\boldsymbol{\mu}}^{(2,0)}$. The characteristic duration is τ_c, the characteristic velocity is v_c and the average velocity of the instantaneous spatial centroid is $\mathbf{v_0}$. The velocity v_c can range from 1 to 2 times the actual rupture velocity [*McGuire et al.*, 2002]. A directivity ratio is defined by $|\mathbf{v_0}|/v_c$, such that ruptures with directivity ratios $\leq$0.5 are predominantly bilateral, while those greater than ~0.5 are predominantly unilateral.

[11] Figure 1 demonstrates the relationship between the characteristic rupture dimensions and the slip distribution of the 2000 western Tottori earthquake. The second moments were calculated directly from the slip model of *Iwata et al.* [2000]. The ellipse represents the area on the fault plane that released the majority of the seismic moment during the earthquake as measured by the second spatial moment. The arrow indicates the rupture directivity, which is described by the mixed moment.

[12] We estimate the second moments by comparing point source synthetic and observed seismograms. The data seismogram recorded at station/component p can be expressed as

$$s_p(\mathbf{x},t) = \int\int G_{ij}^p(\mathbf{x},\mathbf{x}',t-t')\hat{\mathbf{M}}_{\mathbf{ij}}\dot{f}(\mathbf{x}',t')dx'dt' \tag{8}$$

where $\hat{\mathbf{M}}_{\mathbf{ij}}$ is the moment tensor, assumed constant during the earthquake, that describes fault orientation; $\dot{f}$ is the source-space-time function; and G_{ij}^p is the Green's function.

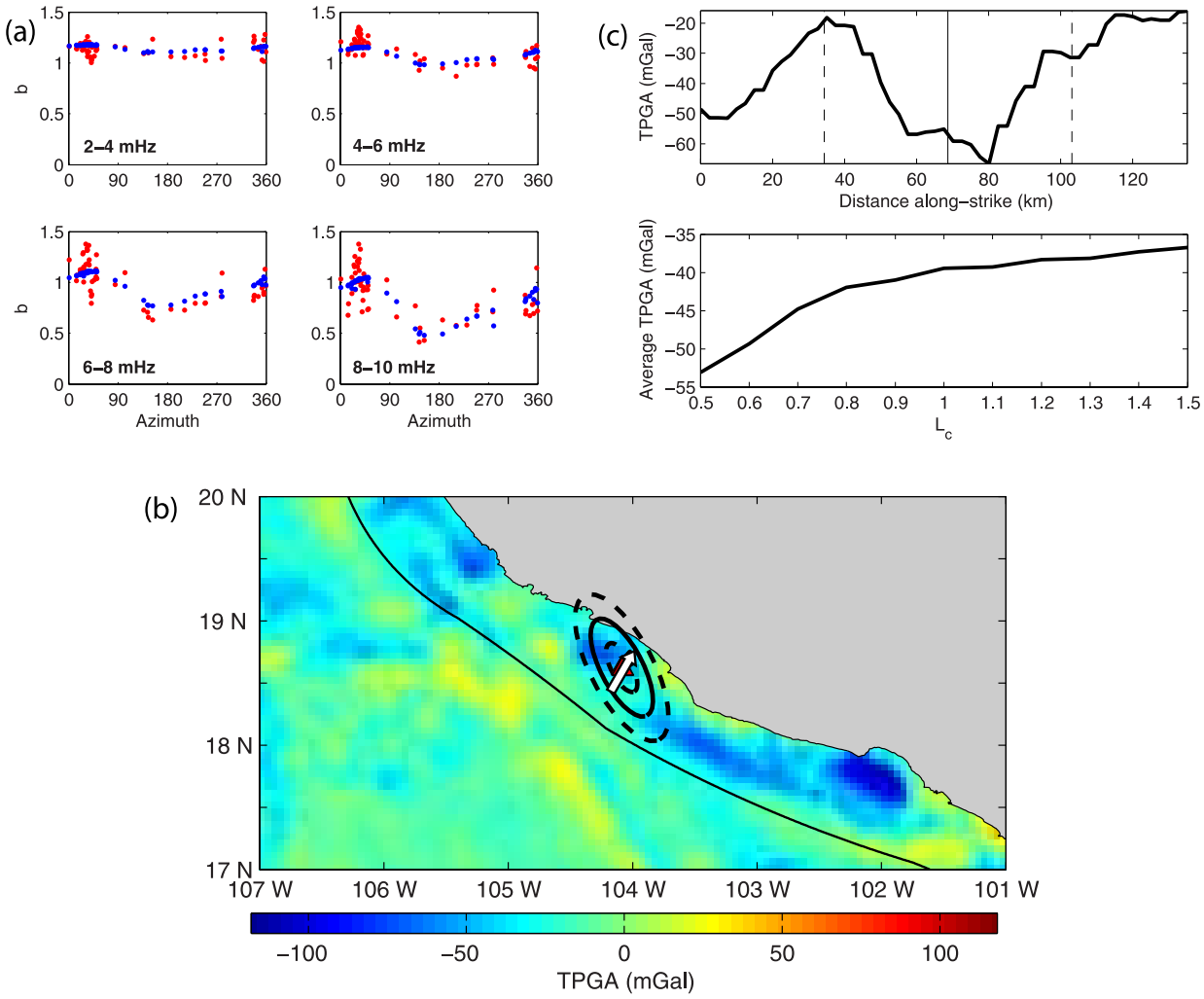

Figure 4. Results for bilateral event 20030122 in Mexico. (a) Amplitude measurements (red) and fit from inversion (blue) at different frequency bands. (b) Centroid (red triangle) and characteristic rupture ellipses with major axes of length 0.5 L_c (inner dashed ellipse), 1 L_c (solid black ellipse) and 1.5 L_c (outer dashed ellipse) plotted on a TPGA map. Directivity vector $\mathbf{v_0}$ is shown by the white arrow. The trench is the thin black line. The area of high seismic moment release is largely contained in a negative TPGA region that corresponds with the Manzanillo fore-arc basin. (c) (top) TPGA values in a single profile along strike of the characteristic rupture ellipse. Rupture propagates from the centroid (solid black line) out to both the left and right. Dashed lines mark the extent of the 1 L_c rupture ellipse. The ends of the plot mark the extent of the 1.5 L_c rupture ellipse. (bottom) Average TPGA measured over rupture ellipses of varying L_c. TPGA is minimized near the centroid (shown by the 0.5 L_c rupture ellipse). Rupture extent (1 L_c) corresponds with increasing TPGA.

The Green's function can be expanded in a Taylor series about a point $(\mathbf{x'_0}, t'_0)$:

$$G^p_{ij}(\mathbf{x},\mathbf{x}',t-t') = \left[1 + (\mathbf{x}'-\mathbf{x}'_\mathbf{0})\cdot\nabla_s + (t'-t'_0)\frac{\partial}{\partial t'_0} + \frac{1}{2}(t'-t'_0)^2\frac{\partial^2}{\partial t'^2_0} + (t'-t'_0)(\mathbf{x}'-\mathbf{x}'_\mathbf{0})\cdot\nabla_s\frac{\partial}{\partial t'_0} + \frac{1}{2}(\mathbf{x}'-\mathbf{x}'_\mathbf{0})^T(\mathbf{x}'-\mathbf{x}'_\mathbf{0}):\nabla_s\nabla_x + \ldots\right] \cdot G^p_{ij}(\mathbf{x},\mathbf{x}'_\mathbf{0},t-t'_0) \quad (9)$$

At low frequencies, the Taylor series can be truncated after the second-order terms allowing the seismogram to be written in terms of the zeroth, first, and second moments:

$$s_p(\mathbf{x},t) = \mu^{(0,0)}G^p_{ij}(\mathbf{x},\mathbf{x}'_\mathbf{0},t-t'_0)\hat{\mathbf{M}}_\mathbf{ij} + \mu^{(1,0)}\cdot\nabla_s G^p_{ij}(\mathbf{x},\mathbf{x}'_\mathbf{0},t-t'_0)\hat{\mathbf{M}}_\mathbf{ij} + \mu^{(0,1)}\frac{\partial}{\partial t'_0}G^p_{ij}(\mathbf{x},\mathbf{x}'_\mathbf{0},t-t'_0)\hat{\mathbf{M}}_\mathbf{ij}$$

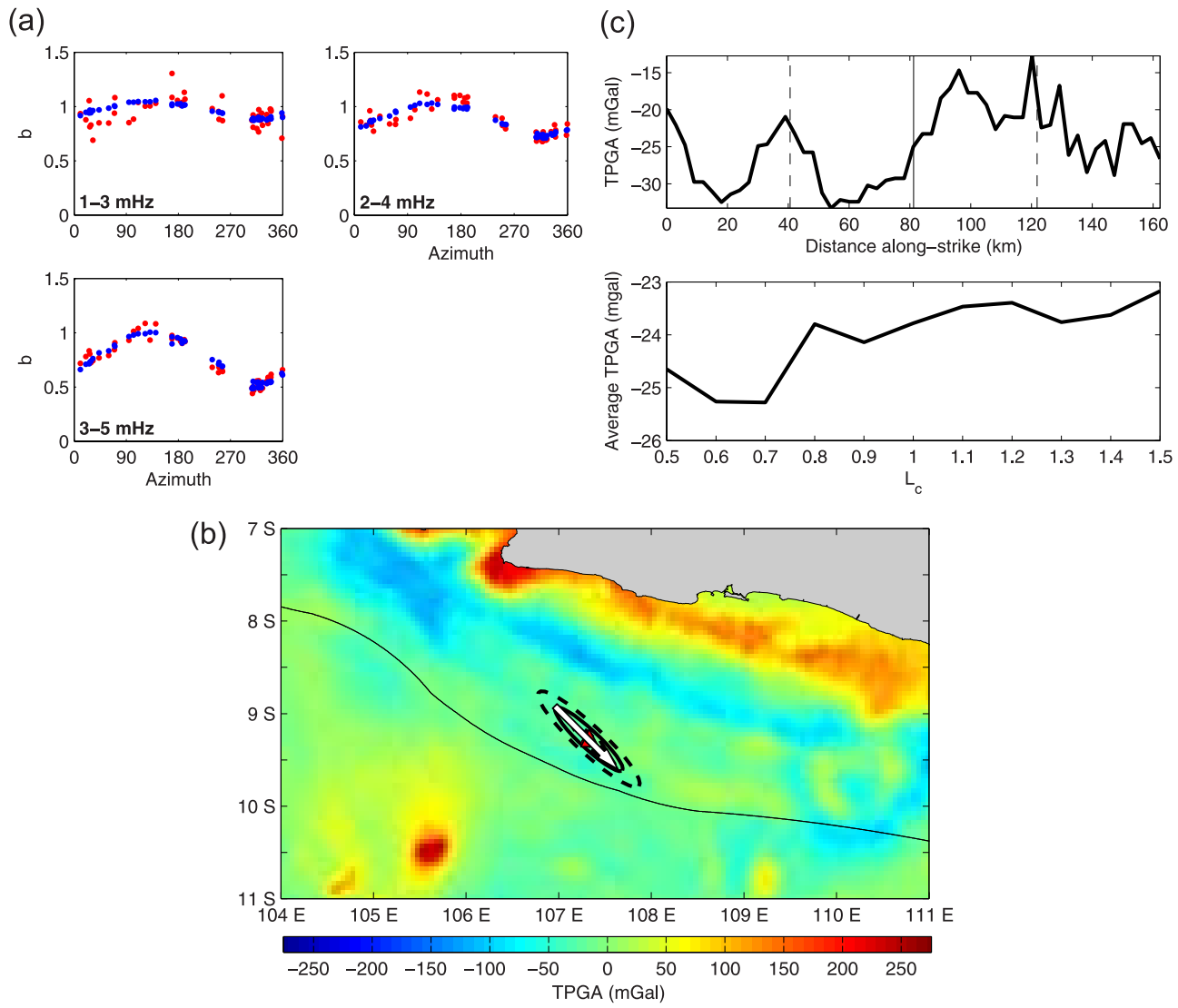

Figure 5. Results for unilateral event 20060717 in Java. (a) Amplitude measurements (red) and model (blue). (b) See Figure 4 for symbol explanation. The area of high seismic moment release shown by the characteristic rupture ellipse (solid black line) stops at a positive TPGA area. (c) (top) TPGA values along strike of the characteristic rupture ellipse. Rupture propagates from left to right. Solid black line denotes the centroid location; dashed lines mark the extent of the 1 L_c rupture ellipse, which occurs as the TPGA becomes more positive. The ends of the plot mark the extent of the 1.5 L_c rupture ellipse. (bottom) Average TPGA measured over rupture ellipses of varying L_c. TPGA is a local minimum at the centroid location (0.5 L_c).

$$+\frac{1}{2}\mu^{(0,2)}\frac{\partial^2}{\partial t_0'^2}G_{ij}^p(\mathbf{x},\mathbf{x}_0',t-t_0')\hat{\mathbf{M}}_{\mathbf{ij}}$$
$$+\mu^{(1,1)}\cdot\nabla_s\frac{\partial}{\partial t_0'}G_{ij}^p(\mathbf{x},\mathbf{x}_0',t-t_0')\hat{\mathbf{M}}_{\mathbf{ij}}$$
$$+\frac{1}{2}\boldsymbol{\mu}^{(2,0)}:\nabla_s\nabla_s G_{ij}^p(\mathbf{x},\mathbf{x}_0',t-t_0')\hat{\mathbf{M}}_{\mathbf{ij}} \quad (10)$$

The first term of the equation on the right-hand side is the point source synthetic seismogram, $\tilde{s}_p = \mu^{(0,0)}G_{ij}^p(\mathbf{x}, \mathbf{x'_0}, t - t'_0)\hat{\mathbf{M}}_{\mathbf{ij}}$. Thus the observed seismogram is described by the contribution from the best fitting point source perturbed by finite source effects.

[13] The perturbations to the synthetic seismogram that describe the finite source can be estimated from the data using (10). To measure these anomalies, we rewrite (10) as $s_p(\mathbf{x}, t) = \sum m_i A_{pi}(t)$, where $\mathbf{m}$ is a vector containing the independent elements of the zeroth, first, and second moments, and $A_{pi}(t)$ is the partial derivative of the Green's function specific to the ith element of $\mathbf{m}$. Then the cross-correlation function of s and $\tilde{s}_p$ can be expressed as

$$C_{s\tilde{s}}(\tau) = s_p(t)\otimes\tilde{s}_p(t-\tau) \approx \tilde{s}_p(t-\tau)\otimes\sum_i m_i A_{pi}(t)$$
$$= \sum_i m_i\tilde{s}_p(t-\tau)\otimes A_{pi}(t) \quad (11)$$

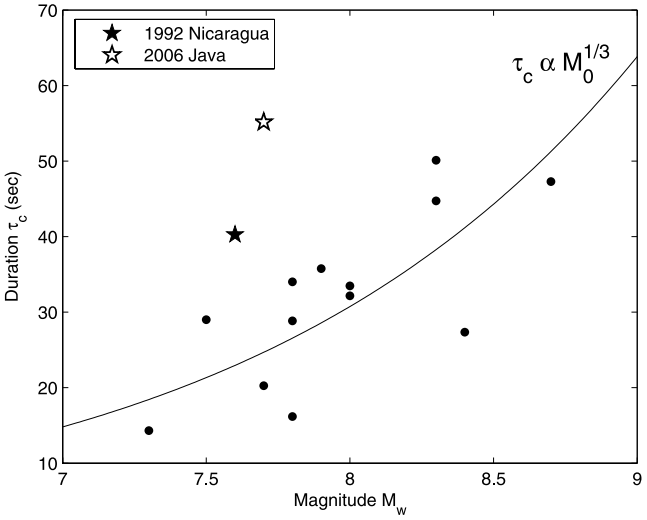

Figure 6. M_w versus duration for events in the data set, with a least squares fit showing the scaling between moment and duration. The 1994 Nicaragua and 2006 Java tsunami earthquakes show anomalously long durations for events of their magnitudes.

A system of equations $\mathbf{A_{pj}m_j} = b_p$ can then be defined, where the measurement b_p is the peak of the cross-correlogram $C_{s\tilde{s}}$ at station p, and $\mathbf{A_{pj}}$ is the cross correlation of $A_{pj}(t)$ with synthetic seismogram $\tilde{s}_p(t - \tau_p)$. We weight both b_p and $\mathbf{A_{pj}}$ by the peak of the autocorrelogram of $\tilde{s}_p$ to account for arbitrary differences in amplitude between stations. Thus, in our measurement scheme $b < 1$ implies that the observed seismogram has a lower amplitude than the point source synthetic, as would be expected if the arrival is sensitive to the destructive interference associated with finite source effects in the frequency band being considered. This measurement scheme provides a straightforward way to identify the directivity of an earthquake. Figure 2 shows the amplitude measurements made from a synthetic line source test simulating rupture propagating toward the east. Low amplitude measurements ($b < 1$) are found at azimuths of around 270, away from the direction of propagation.

[14] We measured frequency-dependent amplitude anomalies using fundamental mode Rayleigh wave data obtained from the GSN, GEOFON, GEOSCOPE, MEDNET, and China Digital seismic networks through the IRIS Data Management Center. The point source synthetics for an event were generated using the Global centroid moment tensor (CMT) solution for that event, available at http://www.globalcmt.org. We utilized two sets of point source synthetics: normal mode synthetics, using the one-dimensional (1-D) PREM Earth model [*Dziewonski and Anderson*, 1981] with phase velocity maps correcting for 3-D structure [*Ekstrom et al.*, 1997]; and 3-D synthetics, calculated using the spectral element method of *Komatitsch and Tromp* [1999] with the 3-D velocity model CRUST2.0 [*Bassin et al.*, 2000] and mantle velocity model S20RTS [*Ritsema and van Heijst*, 2000]. We used the 1-D normal mode synthetic seismograms to calculate $\mathbf{A_{pj}}(t)$, the partial derivatives of the Green's functions. These derivatives depend primarily on source-station geometry and so the accuracy of the velocity model is not as important as it is for the amplitude measurements, which we therefore made using the 3-D synthetic seismograms. The improvement in Earth model allowed much more accurate amplitude predictions to be made for the Rayleigh wave, especially at the higher-frequency bands used in this study (see Appendix A for further discussion regarding the use of 1-D versus 3-D synthetics).

[15] For each event, we make measurements at a set of global stations with good azimuthal coverage and at a number of frequency bands ranging from 1 to 10 mHz. Waveforms are windowed around the peak of the Rayleigh wave using frequency-dependent window lengths prior to cross correlation. Stations with correlation coefficients less than 0.9 in any frequency band are discarded from all bands in the inversion to avoid errors from unmodeled heterogeneity. The magnitude of the amplitude anomaly increases with frequency, however, we can only use frequency bands where the amplitude reduction due to finite source effects is less than about 60% of the point source amplitude. Above this band, higher-order terms in (9) become important (Figure 2). The useable frequency range depends on the spatial extent and directivity of the rupture and hence is different for different sized earthquakes.

[16] The inverse problem for the second moments is nonunique but can be stabilized by incorporating the constraint that the 4-D source region must have a nonnegative volume [*Das and Kostrov*, 1997; *McGuire et al.*, 2001]. Other constraints are used to limit changes to the centroid depth as well as ensure that rupture does not occur above the Earth's surface. These nonlinear constraints are expressed as linear matrix inequalities in the semidefinite programming approach of *Vandenberghe and Boyd* [1996]. The least squares objective function (11) is minimized subject to the various inequality constraints. The solution **m** is a 15 component vector containing the second moments as well as changes to the centroid time, location and seismic moment.

[17] We use a leave-one-out jackknife technique to estimate the error of the solution [*Tukey*, 1984]. We divide the data into N subsets, where N is the number of stations. For the ith subset, the measurements at station i in all frequency bands are left out, and the inversion is performed with the remaining data to produce an estimate of the model parameters. The N estimates of the model parameters then provide a conservative estimate of the variance of the model parameters [*Efron and Stein*, 1981]. The variance of the model parameters can then be used in standard error propagation equations to estimate the variance in derived quantities such as L_c and τ_c [*Bevington and Robinson*, 1992].

[18] The characteristic rupture ellipses for each event are compared to the maps of trench- parallel gravity anomaly (TPGA) produced by *Song and Simons* [2003]. To construct these maps, an average trench normal gravity profile for each subduction zone is removed from the free air gravity data [*Sandwell and Smith*, 1997] along the length of the subduction zone. The resulting TPGA illuminates shorter-wavelength features such as fore-arc basins. We compare the characteristic rupture dimensions with the spatial variations in TPGA to test the hypothesis that a correlation exists between variations in the TPGA field and earthquake

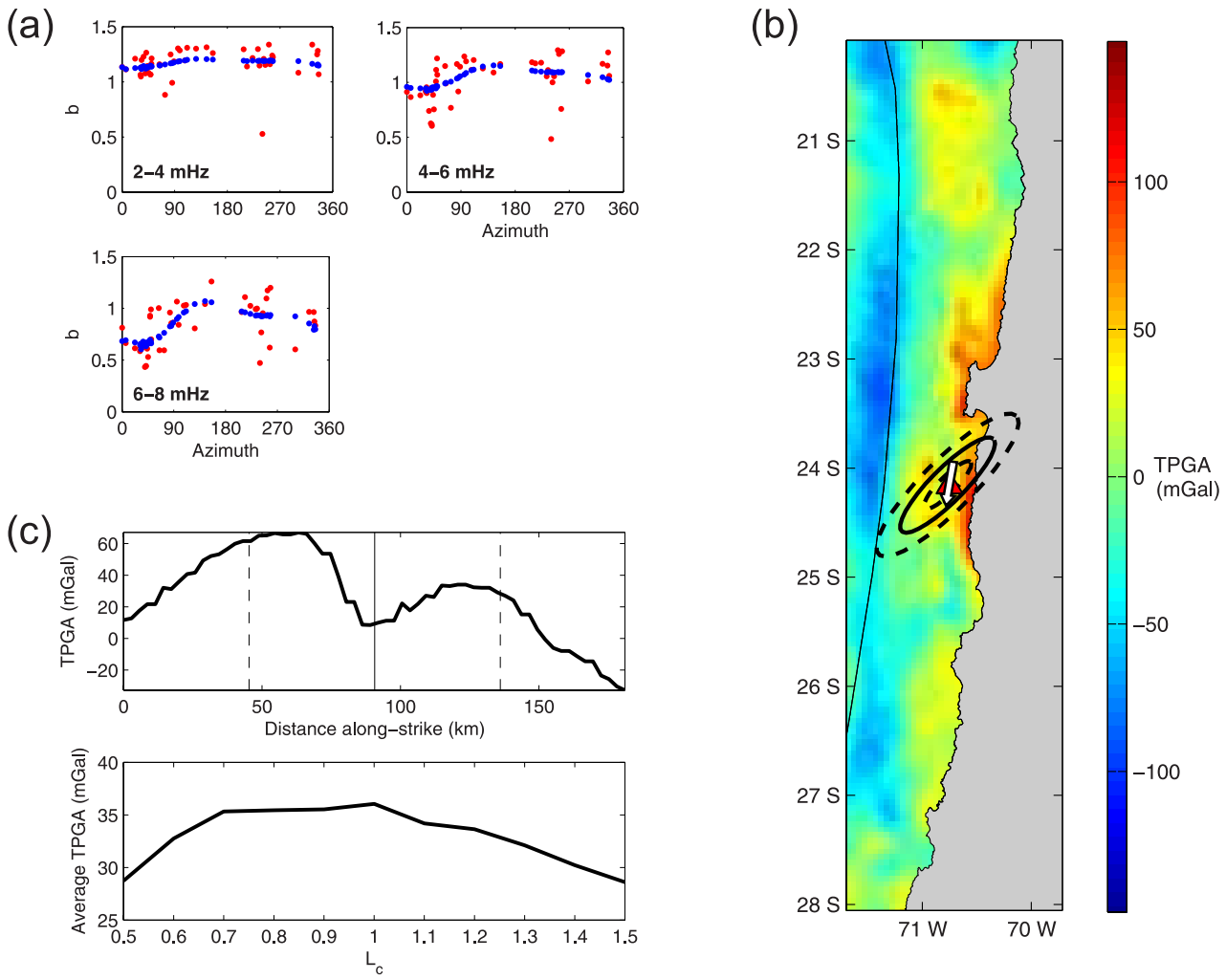

Figure 7. Results for event 19950730 in Chile. (a) Amplitude measurements (red) and model (blue). (b) See Figure 4 for symbol explanation. Although the majority of the seismic moment released in this event occurred in a high TPGA region, the centroid is located in a local TPGA minimum. (c) (top) TPGA values along strike of the characteristic rupture ellipse. Rupture propagates from the centroid (black line) out to the limits of the rupture ellipse (dashed line). The ends of the plot mark the extent of the 1.5 L_c rupture ellipse. TPGA values at along-strike distances of less than 50 km should be ignored because they occur inland, where the TPGA measurements are not as accurate. (bottom) Average TPGA measured over rupture ellipses of varying L_c. Inland TPGA values were masked out in calculating the average. Again a local minimum occurs near the centroid.

rupture characteristics such as centroid location, rupture extent and directivity.

3. Results

[19] We estimated the second moments for 15 shallow thrust earthquakes (M_w > 7.5) that occurred on the plate interface in circum-Pacific subduction zones from 1992 to 2006 (Figure 3). Because of the complex nature of the moment release during the 2004 Sumatra earthquake, this event was not included in our analysis. Table 1 summarizes the characteristic rupture dimensions of these events and Table 2 summarizes the second moment inversion results. Several representative events are discussed in greater detail below. Appendix B contains our Rayleigh wave measurements and comparisons with the TPGA field for each event.

3.1. The 2003 Colima Mexico Earthquake

[20] On 22 January 2003, a M_w 7.5 earthquake occurred near the state of Colima, Mexico. This event primarily ruptured bilaterally in the updip-downdip directions [*Yagi et al.*, 2004]. Our second moment estimates (Table 1 and Figure 4a) support this conclusion. The inversion resulted in a characteristic rupture length L_c of 92 km, a duration τ_c of 29 s, and a directivity ratio of 0.44. This agrees well with the finite source model determined by *Yagi et al.* [2004] using a joint inversion of teleseismic body wave and strong motion data.

[21] The characteristic rupture ellipse representing the area of greatest moment release is compared to the TPGA field in Figure 4b. Although the measurements and directivity clearly indicate a downdip rupture, the ellipse is oriented more along strike. The centroid is located in a

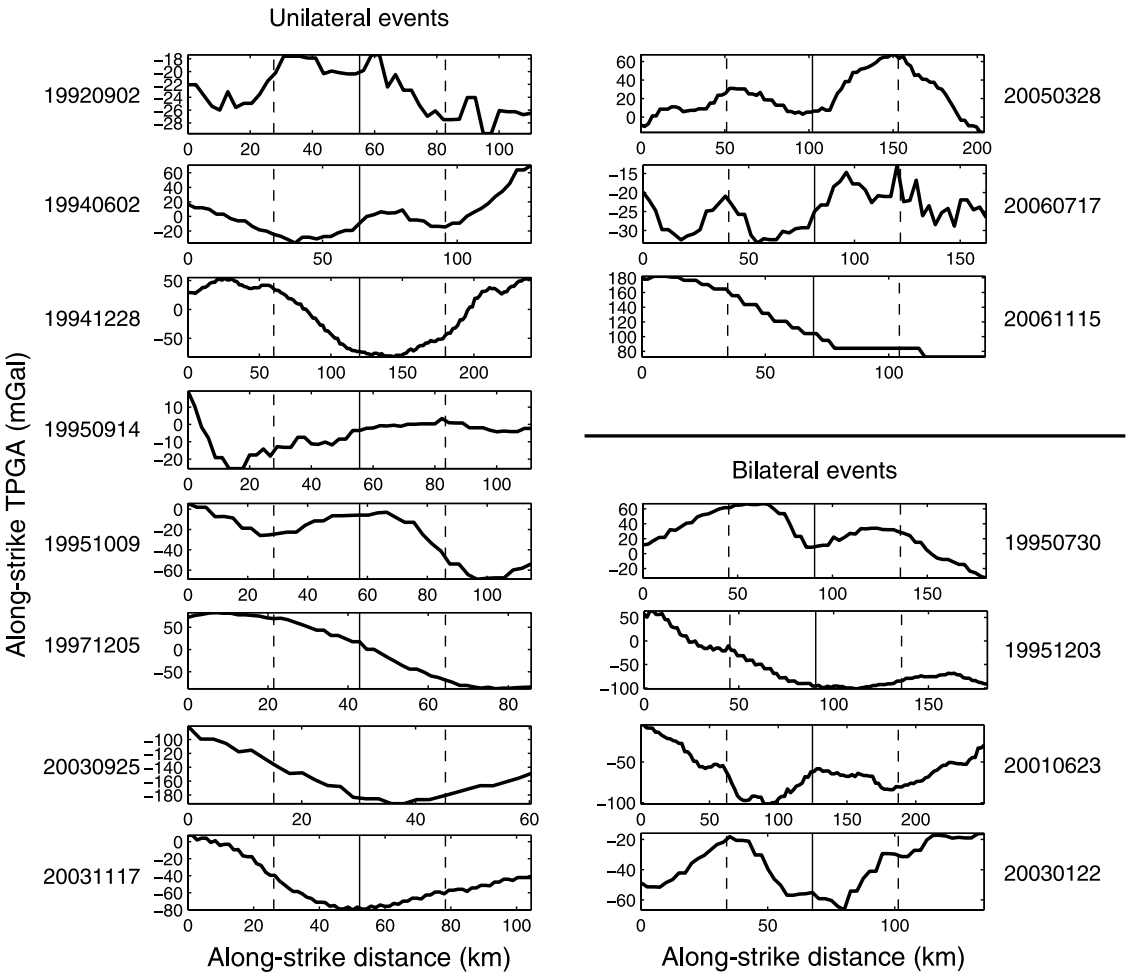

Figure 8. TPGA measured along strike of rupture ellipses for each event in the data set. The solid line marks the centroid location, and the dashed lines mark the extent of the best fitting (1 L_c) rupture ellipse. Rupture propagates from left to right for unilateral events and from the centroid outward in both directions for bilateral events. In general, the rupture ellipse limits correspond with positive changes in TPGA. The profiles of 19950914 and 19950730 are not entirely accurate, as part of each profile occurs on land, where accurate TPGA measurements are unavailable.

highly negative TPGA region which corresponds to the Manzanillo basin [*Wells et al.*, 2003]. This basin also overlies part of the rupture area of the 1995 M_w 8.0 Jalisco event (Figure B7b in Appendix B). The along-strike limits of the rupture ellipse are characterized by local TPGA maxima (Figure 4c). These results suggest that the main moment release filled the area underlying the Manzanillo basin. Figure 4c (bottom) shows the average TPGA over rupture ellipses of varying L_c (with a constant aspect ratio), which illustrates how the TPGA changes within the rupture zone. The average TPGA is minimized near the centroid and increases as the region near the boundary of the actual rupture area is included (i.e., 1 L_c in Figure 4c). Therefore the limits of the significant moment release are characterized by increasing TPGA.

3.2. The 2006 Java Earthquake

[22] On 17 July 2006, a M_w 7.7 earthquake occurred in the fore arc of the Java trench. This earthquake generated a tsunami with a wave height of 1.8 m that struck the coast of Java, killing over 400 people. Preliminary results reported by the U.S. Geological Survey (USGS) (http://earthquake.usgs.gov/eqcenter/eqinthenews/2006/usqgaf) suggest that this event had a similar source mechanism as that of the M_w 7.8 shallow thrust earthquake (also in this study) that occurred off the coast of Java on 2 June 1994 which also generated a tsunami.

[23] For this event, we generated point source synthetics using the focal mechanism reported in the Global CMT catalog but the centroid location reported by the USGS. In their study of the 1994 Java earthquake, *Abercrombie et al.* [2001] found that the Global CMT locations for earthquakes in the Java trench appear to be systematically biased to the south and suggest that the 3-D velocity models used in the CMT inversion are inadequate in this part of the globe.

[24] There is a very strong directivity signal at azimuths of around 300 (Figure 5a), indicating that rupture propagated unilaterally to the east-southeast. By the 3–5 mHz band, the amplitude of the data has dropped to 0.5 of the amplitude of the synthetic. Such a strong signal in this low of a frequency band is more typical of M_w 8.5 events

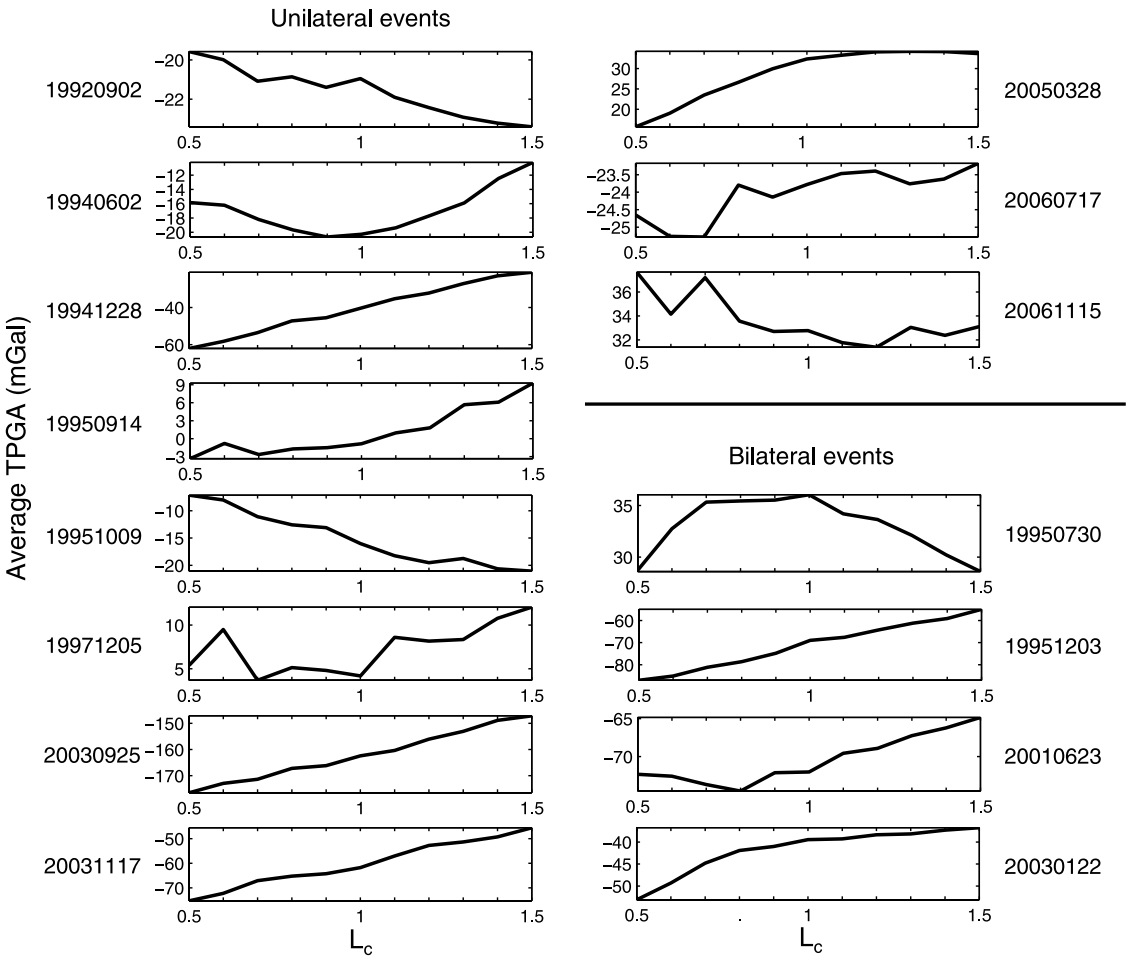

Figure 9. Average TPGA over rupture ellipses of varying L_c for each event of the data set. In general, the average TPGA increases with L_c, indicating the centroid (reflected by the rupture ellipse of 0.5 L_c) was located in a local TPGA minimum. The limits of the rupture ellipses which occur at 1 L_c generally coincide with increases or maxima in the TPGA.

than M_w 7.7 events (compare with measurements for a M_w 7.5 earthquake shown in Figure 4a and measurements for a M_w 8.7 shown in Figure B14). The inversion for the second moments resulted in a length L_c of 108 km, a duration τ_c of 55 s, and an average instantaneous centroid velocity $|\mathbf{v_0}|$ of 1.9 km/s. The characteristic rupture length, relatively long duration and directivity are consistent with other slip models for this event [*Ammon et al.*, 2006; *Fujii and Satake*, 2006]. The duration is surprisingly long for an event of this magnitude; the duration for the M_w 7.5 Mexico earthquake was only 29 s. The duration and moment for each event in this study are shown in Figure 6, fit with a line illustrating the scaling of duration as the cube root of moment. Both this event and the 1992 Nicaragua event have anomalously long durations considering their magnitudes. This shows these earthquakes belong to a class of slow tsunami earthquakes that radiate a large amount of low-frequency energy relative to their high-frequency radiation [e.g., *Polet and Kanamori*, 2000]. However, there is nothing obviously different about the TPGA profiles for these two events compared to the other events (e.g., Figure 4). Thus we find no evidence in this study to suggest a direct relationship between structure in the TPGA field and tsunamigenic potential.

[25] Figure 5b compares the characteristic rupture ellipse to the TPGA field. The centroid is again located in a negative TPGA region, and the limits of the rupture ellipse occur as the TPGA becomes increasingly positive (Figure 5c). When we consider the average TPGA over varying rupture dimensions, we find that the TPGA increases slightly near the edges of the rupture but is essentially flat. Hence the unilateral rupture propagation to the east appears to have been stopped near a local TPGA maximum (Figures 5b and 5c).

3.3. The 1995 Chile Earthquake

[26] A M_w 8.0 earthquake occurred off the northern coast of Chile near the town of Antofagasta on 30 July 1995. This event has been the subject of a number of studies, which generally found that rupture initiated just south of the Mejillones peninsula and propagated unilaterally to the southwest [e.g., *Delouis et al.*, 1997; *Ihmlé and Ruegg*, 1997; *Carlo et al.*, 1999; *Pritchard et al.*, 2006]. Our measurements and model fit are shown in Figure 7a. The inversion resulted in an L_c of 121 km, a τ_c of 33 s, and a

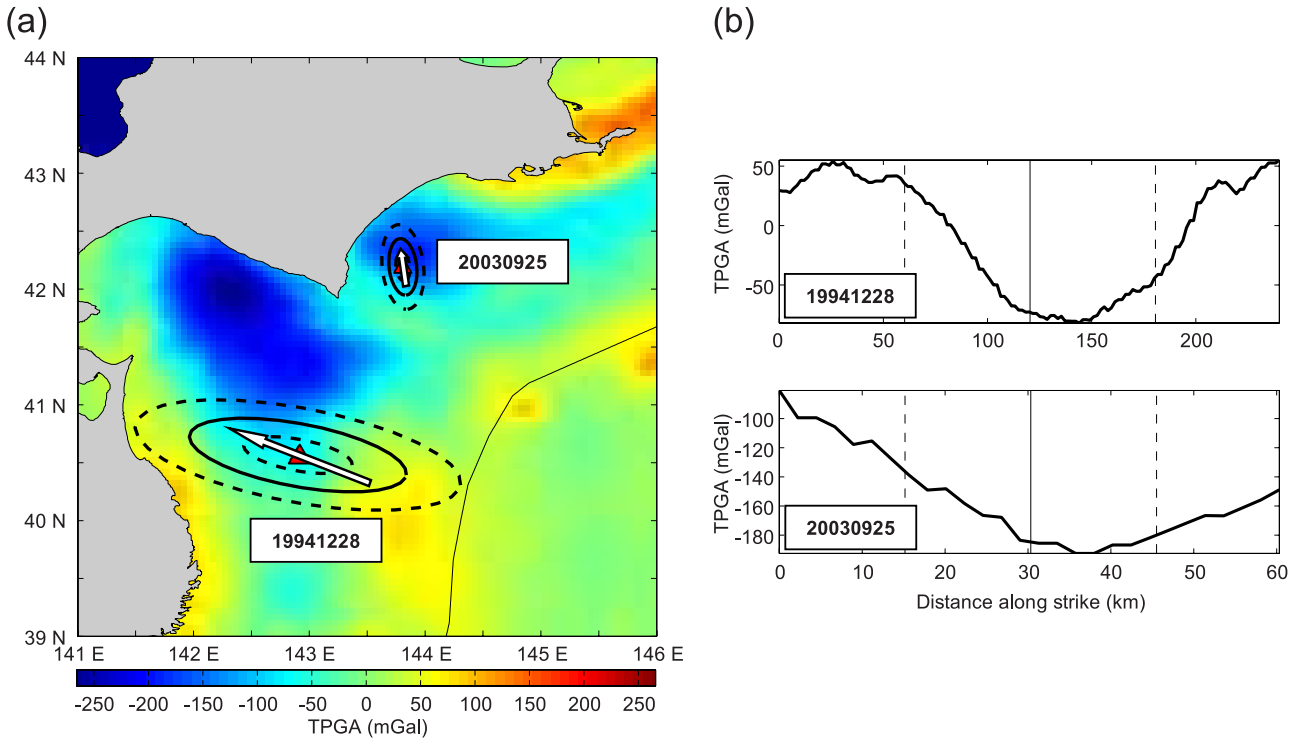

Figure 10. (a) Rupture ellipses for events 19941228 and 20030925 off the coast of northeastern Japan plotted on TPGA. See Figure 4 for symbol explanation. (b) Along-strike TPGA values for (top) 19941228 and (bottom) 20030925. Both events ruptured unilaterally, so rupture progresses from left to right. The 1 L_c limit in both cases correspond with a positive TPGA slope that can be qualitatively correlated with transitions from velocity-weakening to velocity-strengthening behavior shown in maps from *Miyazaki et al.* [2004b] and *Nishimura et al.* [2004].

directivity ratio of 0.33, revealing a somewhat surprising bilateral component to the rupture. Our centroid location and rupture length are consistent with other slip models [*Ihmlé and Ruegg*, 1997; *Pritchard et al.*, 2006], although the orientation of the moment release is slightly different. Where other slip models are oriented predominantly along strike, our rupture ellipse is oriented at around a 45° angle to the trench. However, had our rupture ellipse been oriented more along strike, the overall shape of the TPGA profile would not change significantly, as the centroid is surrounded by higher TPGA regions along strike as well as updip and downdip (Figure 7b).

[27] The main moment release of this event, unlike most of the others in this study, was located in a positive TPGA region, although the centroid was located in a local TPGA minimum (Figure 7b). These higher TPGA regions are associated with the Mejillones Peninsula to the north and the Antofagasta Ridge to the west, both of which are thought to be tilted fault blocks [*von Huene and Ranero*, 2003]. The local TPGA minimum in which the centroid is located corresponds with a sediment-ponded basin behind the Antofagasta Ridge. The TPGA profiles show that the 1 L_c limit occurs near the high positive TPGA region denoting the Antofagasta Ridge (Figure 7c). However, had rupture continued beyond 1 L_c, the TPGA would have decreased and so, unlike most of the other events in the data set, there is no obvious correlation between positive changes in the TPGA field and the termination of rupture.

3.4. Evaluation of Bias From Unmodeled Propagation Effects

[28] If inadequacies of the 3-D Earth models result in a significant bias in our estimates of rupture area, this bias should be shared by earthquakes within a given subduction zone owing to the very long wavelength nature of the R1 waves we utilize. Our data set consists of events from essentially four regions: the northwest Pacific (six events), the Middle American trench (four events), the Java trench (three events), and the Peru-Chile trench (two events). We have utilized two approaches to check for bias in our estimated rupture areas. First, many events have been compared to slip distributions derived from local geodetic data. For instance, our rupture areas agree well with geodetic inversions for both the 2003 Tokachi-oki [*Miyazaki et al.*, 2004a] and 1995 Jalisco events [*McGuire et al.*, 2001]. Moreover, there is considerable variability in the rupture directivity inferred for the various northwest Pacific earthquakes indicating that systematic biases are relatively unimportant for the majority of our events. As a further check to ensure that propagation effects do not bias the results, we compared our results to those obtained using an empirical Green's function (EGF) instead of point source synthetics to make amplitude measurements. In general, theoretical Green's functions (TGF) are preferable because of their superior signal-to-noise ratio at low frequencies and their true point source nature in time, but EGFs provide a useful way to check for consistency. Examples of EGF measure-

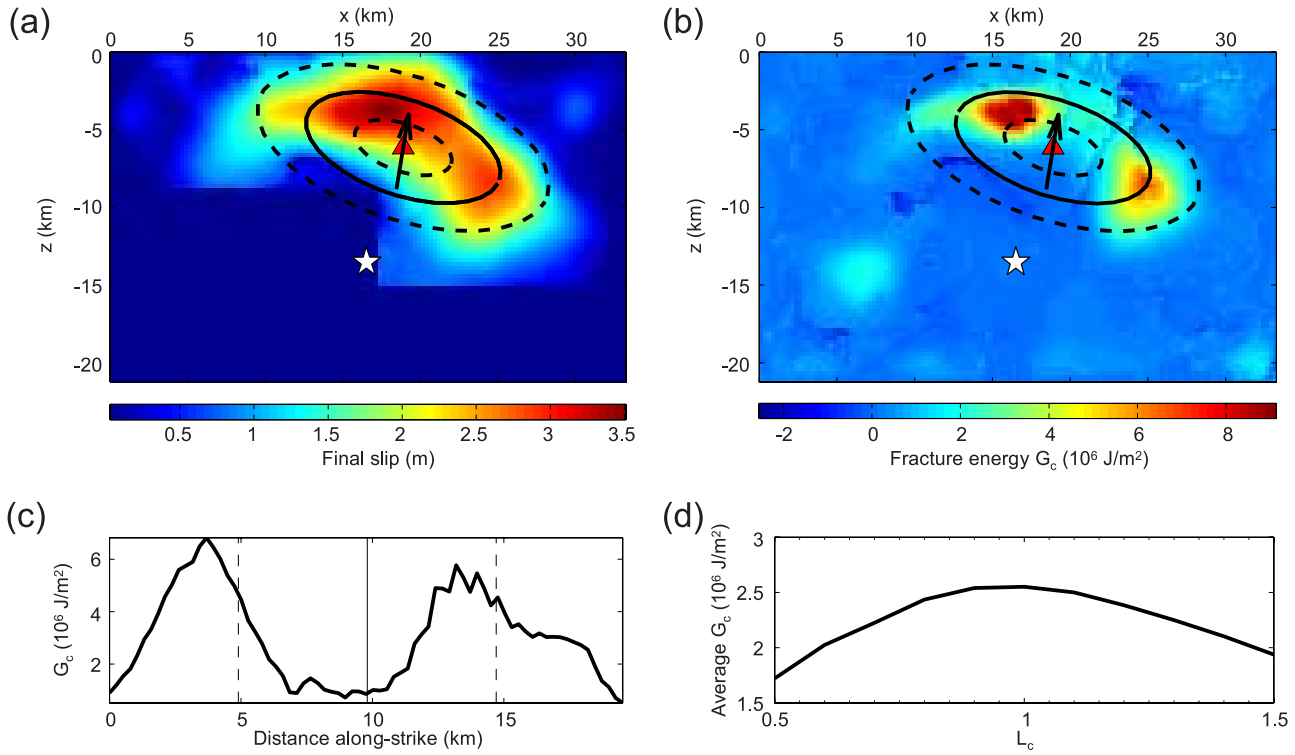

Figure 11. (a) Rupture ellipse (solid black ellipse) for the 2000 Tottori event plotted on the slip model of *Iwata et al.* [2000] from which it was determined. Ellipses of length 0.5 and 1.5 L_c are also shown (inner and outer dashed ellipses, respectively). Centroid location is marked by the red triangle. Directivity is indicated by the arrow. Hypocenter location marked by the white star. (b) Rupture ellipses and directivity plotted on top of fracture energy G_c calculated by *Dalguer et al.* [2002]. (c) G_c along the axis of the rupture ellipse. Maxima occur near the rupture ellipse limits (dashed lines). A minimum occurs at the centroid (solid black line). (d) Average G_c over ellipses of varying L_c. Maximum occurs near 1 L_c. Centroid occurs at a local minimum.

ments and inversion results for a northwest Pacific event and the two Peru-Chile trench events can be found in Appendix B (Figures B4, B5, and B11). The two Peru-Chile trench events have ~15° and 55° rotations of their rupture ellipses when using EGFs versus TGFs, indicating that unmodeled effects may bias our estimates of rupture area for this subduction zone. We are not confident that the EGF results are better because of the large amount of scatter (e.g., poor SNR) at frequencies below 5 mHz for these events (Figure B5a and B11a). The TPGA profile changes qualitatively for only the 2001 Peru event.

3.5. Summary of Results

[29] Our survey of 15 earthquakes indicates that TPGA increases as a rupture approaches the edge of its eventual rupture patch. Figures 8 and 9 summarize the along-strike TPGA and average TPGA profiles for all of the events. In 11 of the 15 events, the centroid was clearly located where the TPGA is a local minimum. In most cases this value was negative (e.g., events 19941228, 20030122), but in some cases it was positive (e.g., events 20050328, 19950730). The magnitude of TPGA variation over the rupture area also differs from event to event. In some cases, the average TPGA varied over a range of ~2 mGal, while for others variations occurred over a range of ~40 mGal (see events 20060717 and 19941228 in Figure 9). This suggests that the relative rather than absolute values of TPGA may reflect rupture behavior more directly.

[30] Our results also show that in 11 of the 15 events, the limits of the rupture ellipses correspond with increasing TPGA (Figure 9). In 3 events, the TPGA is essentially flat between the centroid and the rupture edges. In one event (19951009), the limits correspond with decreasing TPGA, and so the reason for rupture to stop is not apparent in the TPGA field. If we exclude the South American events due to uncertainties in propagation effects, 9 of 13 events have increasing TPGA. Thus, in the majority of the events in our data set, the 1 L_c limit corresponds with a positive gradient in TPGA (Figure 9). This suggests that a relationship exists between the TPGA field and physical conditions on the plate interface that control the extent of individual ruptures.

4. Discussion

[31] In agreement with previous studies [*Song and Simons*, 2003; *Wells et al.*, 2003], our results demonstrate that the areas of greatest seismic moment release for large subduction zone earthquakes tend to occur beneath local minima in the TPGA field. Typically these minima denote the presence of a fore-arc sedimentary basin. Additionally, we demonstrated that the limits of the two-dimensional rupture areas correlate with positive gradients of TPGA

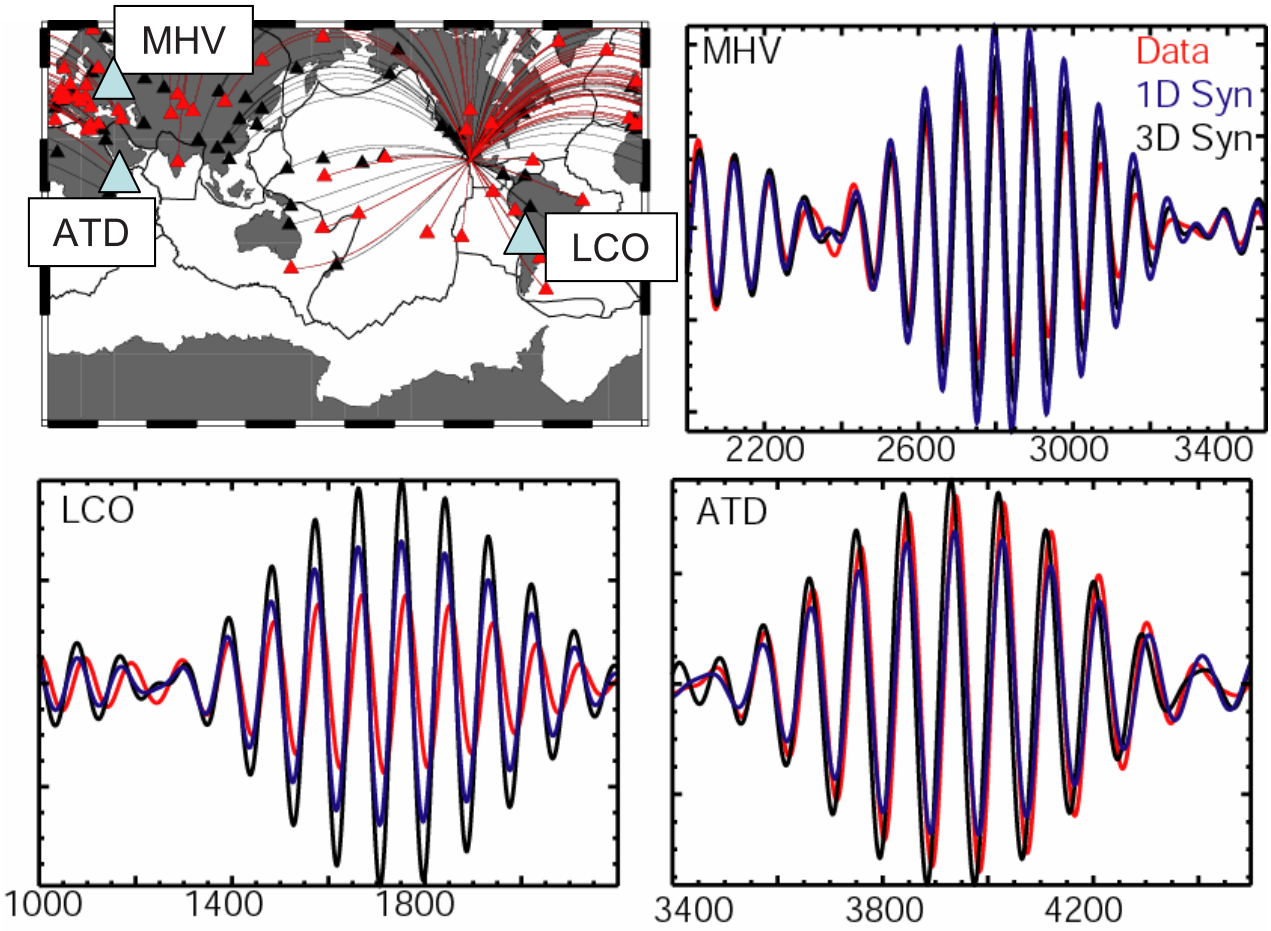

Figure A1. (top left) Map showing great circle paths from the source of the 2003 Mexico earthquake to stations. Red stations were used in the final inversion. Comparison of 1-D and 3-D synthetic waveforms at stations MHV, LCO, and ATD (blue triangles on the map) to actual data in the 10–12 mHz band. The amplitude measurements are markedly different, especially at LCO.

(Figure 9). Our observations lead to two primary conclusions regarding the connection between TPGA and the frictional conditions on the plate interface. First, the relative rather than absolute values of TPGA have the greatest correlation to individual rupture behavior. Second, there appears to be a correlation between the resistance to rupture growth (either spatial variations in current shear stress level or material properties) and the edges of local TPGA minima. Although these minima often correlate with fore-arc basins, they do not identify them uniquely because of other variations in seafloor topography and density which contribute to the gravity field. However, *Wells et al.* [2003] demonstrated that the basin edges are spatially correlated with maxima in gravity gradient rather than absolute values of the free air gravity field, which they then correlate with updip and downdip frictional stability transitions. In this section, we further explore the potential mechanisms connecting the upper plate fore-arc basins reflected in the TPGA field and the resistance to rupture propagation observed to occur near the edges of these basins.

4.1. Fore-Arc Basin Formation and Wedge Mechanics

[32] A number of 2-D models have examined the link between fore-arc basin formation and conditions along the plate interface. *Byrne et al.* [1988] suggested that the presence of fore-arc basins indicates strong material at depth which causes a change in the critical taper angle of the wedge and allows backstops and outer-arc highs to form which trap sediments. Recent numerical work has explored the mechanics of the upper plate that allow the formation of fore-arc basins [*Fuller et al.*, 2006; *Wang and Hu*, 2006]. *Wang and Hu* [2006] divide the fore arc into an undeforming inner wedge and an actively deforming outer wedge. The inner wedge provides a stable platform for fore-arc basins to form on and overlies the velocity-weakening seismogenic zone, while the outer wedge overlies the velocity-strengthening region updip of the seismogenic zone. *Fuller et al.* [2006] also suggest that fore-arc basins tend to form in stable wedges, and the lack of deformation in such wedges could mean that permeability is reduced in the direction normal to the plate interface, allowing processes such as thermal pressurization to generate elevated pore pressures that could significantly weaken the fault [*Wibberley and Shimamoto*, 2005]. *Song and Simons* [2003] infer that strongly negative TPGA values correlate with increases in the shear traction on the plate interface. Large shear tractions tend to result in more stick-slip behavior [*Marone*, 1998]. While the existing models are fairly simplistic, they

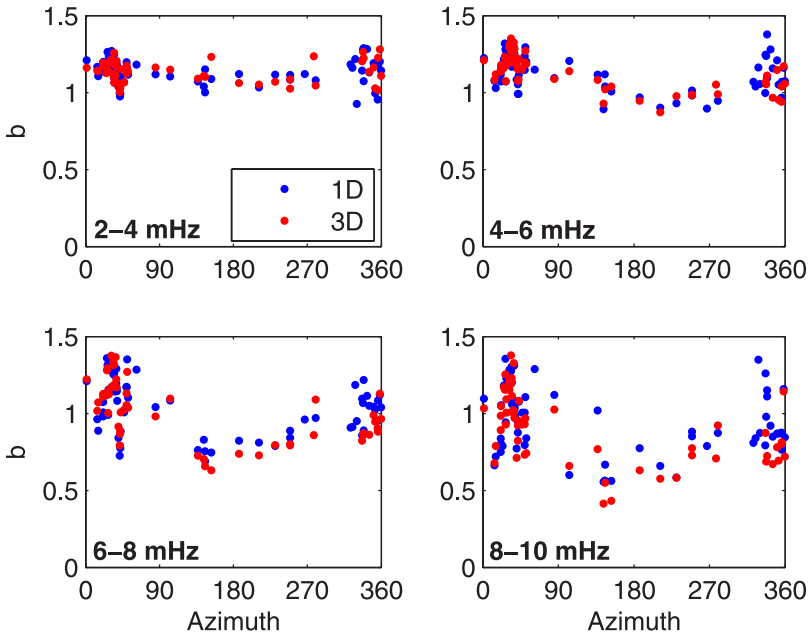

Figure A2. Amplitude measurements in different frequency bands made using 1-D synthetics (blue) and 3-D synthetics (red). At higher frequencies, the measurements become significantly different, particularly in northern azimuths. There is also more scatter in the 1-D synthetic measurements.

demonstrate mechanical reasons to expect fault strength and/or fluid pressure to be different under fore-arc basins than underneath adjacent areas. In general, these frictional differences do not appear to be related to variations in the thermal structure of the plate interface.

4.2. How Great Earthquakes Stop: Dynamic Versus Quenched Heterogeneity

[33] The resistance to rupture growth that causes earthquakes to stop can arise from along-strike variations in shear stress (dynamic heterogeneity) or along-strike variations in fault frictional properties (quenched heterogeneity) [*Guatteri and Spudich*, 2000; *Shaw*, 2000]. In numerical models, time-dependent, dynamic heterogeneities can produce complex earthquake sequences even on faults with uniform frictional properties owing to the low-stress regions leftover from past ruptures [*Shaw*, 2000]. However, the locations of these dynamic heterogeneities vary on the scale of an earthquake cycle (100 s of years). In contrast, the fore-arc basins (and associated TPGA anomalies) reflect the average stress state on the plate interface and within the wedge over timescales of basin formation (at least a million years) [*Fuller et al.*, 2006]. Thus, if large ruptures are stopped simply by encountering the low-stress regions leftover from previous ruptures, as opposed to some long-lived material heterogeneity, then averaging over many earthquake cycles (or equivalently many subduction zones) should remove any correlation with the TPGA field. Our observed correlation between TPGA variations and the boundaries of individual ruptures requires that long-lived, upper plate structural/geological heterogeneity is a first-order control on along-strike rupture extent.

[34] One type of along-strike frictional heterogeneity on a fault that may prevent large throughgoing ruptures are patches of velocity-strengthening material that exist due to compositional or thermal anomalies. The correlation between positive TPGA gradients and a transition from velocity-weakening to velocity-strengthening behavior may be qualitatively assessed in a region such as northeastern Japan. Owing to the dense instrumentation network, a number of studies have mapped the long-term seismogenic behavior of the plate interface in this region [*Miyazaki et al.*, 2004b; *Nishimura et al.*, 2004; *Yamanaka and Kikuchi*, 2004]. Two earthquakes in our study occurred here: the 1994 M_w 7.7 Sanriku-oki earthquake off the coast of northern Honshu (19941228) and the 2003 M_w 8.3 Tokachi-oki earthquake off the coast of Hokkaido (20030925). In their study of the 2003 earthquake, *Miyazaki et al.* [2004b] inferred that the afterslip of this event indicated velocity-strengthening behavior and found that it occurred in areas surrounding the greatest moment release (both along strike and updip). Significant afterslip also occurred in the areas surrounding the greatest coseismic slip of the 1994 Sanriku-oki earthquake [*Nishimura et al.*, 2004].

[35] Our characteristic rupture ellipses for these two events are shown in Figure 10a. For 19941228, the limits of the rupture ellipse occur when the TPGA becomes positive. The positive TPGA regions correspond relatively well with the weak seismic coupling region shown by *Nishimura et al.* [2004]. This observation seems to suggest a correlation between positive TPGA values and velocity-strengthening behavior. However, the rupture ellipse for 20030925 shows that the rupture failed to fill the entire basin and stopped in a negative TPGA region. This suggests the presence of velocity-strengthening materials even though the TPGA remains negative. Instead, the transition from velocity-weakening to velocity-strengthening behavior seems to be correlated with positive TPGA gradients. Beyond the limits of the rupture ellipses for both events,

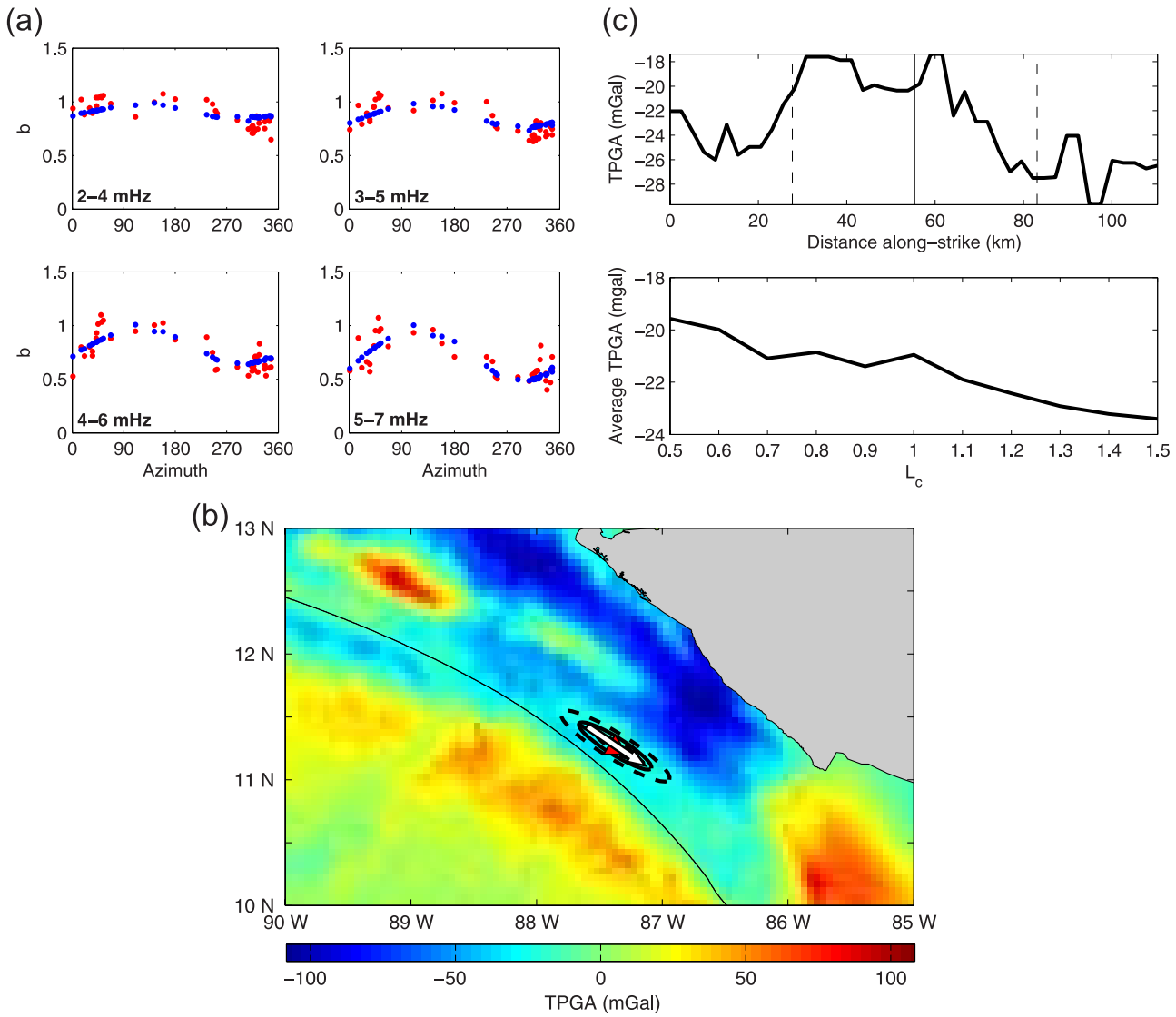

Figure B1. Measurements and results for unilateral event 19940602 in Java. See Figure 4 for symbol explanation.

the TPGA increases (Figure 10b). This change in the TPGA corresponds well in location with changes in the seismic coupling seen in maps drawn by *Nishimura et al.* [2004] and *Miyazaki et al.* [2004b] for the 1994 and 2003 earthquakes, respectively. At least in the Tokachi-oki region, there appears to be a link between increases in TPGA and transitions from velocity-weakening to velocity-strengthening behavior.

[36] A second type of frictional heterogeneity that can play a role in stopping earthquake rupture is regions of velocity weakening material with very high fracture energy. In subduction zones, this may represent areas of increased fault roughness due to the bathymetry of the incoming plate. Figure 11b shows the characteristic rupture ellipse for the 2000 Tottori earthquake plotted on fracture energy calculated by *Dalguer et al.* [2002]. High fracture energies are associated with the limits of the rupture ellipse (Figures 11c and 11d) suggesting that the region near 1 L_c identifies the location of significant resistance to rupture propagation that was necessary to arrest a particular rupture. The fracture energy profiles in Figures 11c–11d are remarkably similar to the typical TPGA profiles found in this study (Figures 8–9) despite being nominally unrelated variables. Thus the variations we observe in TPGA around the 1 L_c portion of the rupture zone may reflect a surprisingly direct connection between the edges of sedimentary basins and the variations in frictional properties of the plate interface.

[37] The primary difference between the fracture energy and frictional stability transitions as explanations for the boundaries of M_w 8 ruptures lies in the role of aseismic slip. In the fracture energy case, most of the plate motion would be expected to be made up by abundant smaller ($M_w < 8$) earthquakes, while in the stability transition explanation, much of the plate motion in these regions could occur aseismically, likely as afterslip. Thus distinguishing between these two types of frozen heterogeneity will require geodetic observations over multiple earthquake cycles, but

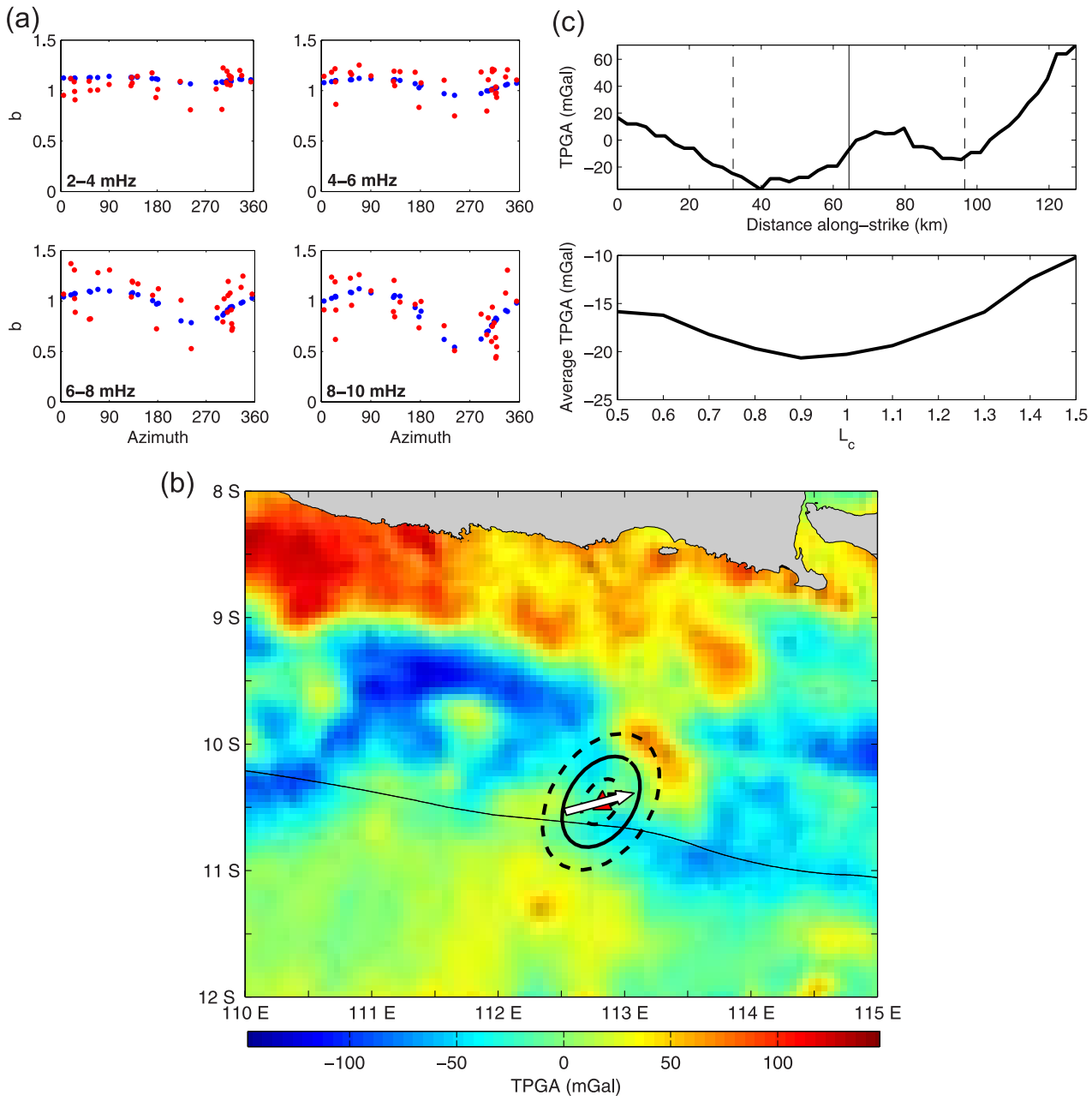

Figure B2. Measurements and results for unilateral event 19941228 in Japan. See Figure 4 for symbol explanation.

at least for the Tokachi-oki region, along-strike variations in frictional stability are important [*Miyazaki et al.*, 2004b].

5. Conclusion

[38] The spatial heterogeneity of frictional properties which cause variations in seismogenic behavior along a subduction zone can be linked to variations in fore-arc TPGA and geological structure [*Song and Simons*, 2003]. To further investigate this relationship, we estimated the rupture characteristics of a global data set of large shallow subduction zone earthquakes and compared them with the TPGA field. The centroid locations typically correspond with local TPGA minima, and the limits of the areas of significant moment release correspond with positive TPGA gradients (Figure 9). These gradients appear to be linked to changes in the frictional properties along the plate interface that control rupture behavior. Owing to the inherently long timescales required for fore-arc basin formation, the correlation between the TPGA field and rupture termination regions indicates that long-lived material heterogeneity rather than short timescale stress heterogeneities are responsible for arresting most great subduction zone ruptures. Variations in TPGA may therefore be used to not only determine the long-term seismogenic behavior along the strike of subduction zones but also to provide estimates of the boundaries of

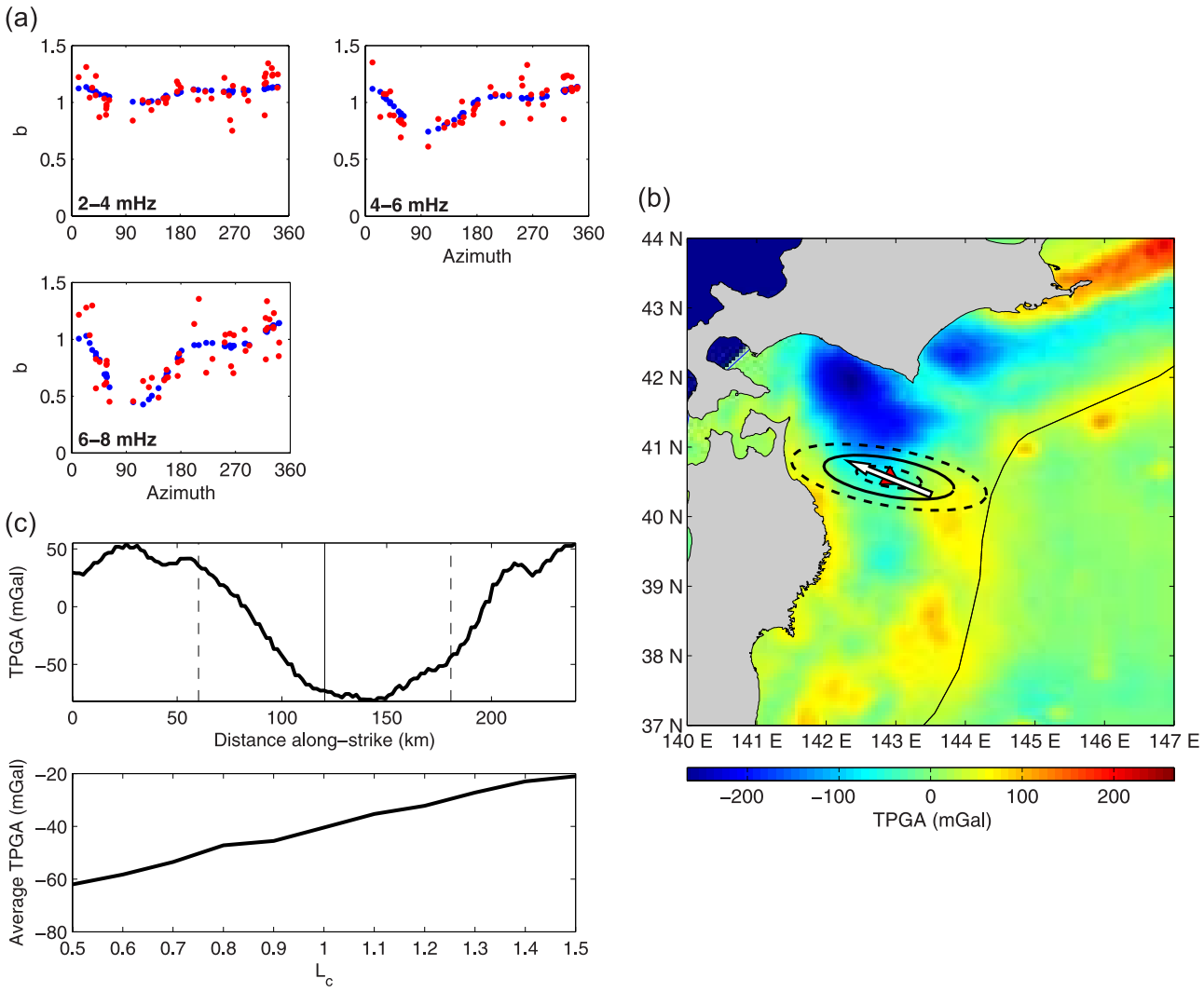

Figure B3. Measurements and results for unilateral event 19950914 in Mexico. See Figure 4 for symbol explanation.

individual future ruptures for probabilistic seismic hazard analysis.

Appendix A: One-Dimensional Versus Three-Dimensional Synthetics

[39] In this appendix, we discuss the reasons for using both 1-D and 3-D synthetic seismograms in this study. We use 1-D normal mode synthetic seismograms to calculate the partial derivatives used in the inversion and 3-D synthetics to make the actual amplitude measurements. The 1-D synthetics are much faster to compute than the 3-D synthetics, which require a 64-processor Linux cluster, and so they are considerably more efficient to use for the numerical calculations of the partial derivatives of the Green's functions. The use of 3-D synthetics rather than 1-D synthetics to calculate the partial derivatives in (10) would make little difference in the inversion results. The partial derivatives are calculated from perturbations in source location, and so are more sensitive to source-station geometry than to the velocity model used to generate the synthetics. The results from a test event confirm that little is gained by using 3-D synthetics for the partial derivatives; therefore, because the 3-D synthetics require much more computational effort, we use the 1-D synthetics to calculate the partial derivatives.

[40] However, the 3-D synthetics produce more accurate R1 amplitude predictions at higher frequencies, so they are used to make the amplitude measurements. The difference in amplitude predictions can be seen by comparing the 1-D and 3-D synthetics with the seismograms observed at three stations at different azimuths for the 2003 M_w 7.5 earthquake in Mexico (Figure A1). Amplitude measurements made using 1-D synthetics would have been lowest at station MHV (az = 21). With the 3-D synthetics, the lowest measurement occurs at station LCO (az = 145), which indicates a completely different direction of rupture directivity.

[41] The magnitude of amplitude anomaly measured with 1-D and 3-D synthetics can also be very different (see station LCO in Figure A1). Figure A2 compares the amplitude measurements made using 1-D and 3-D synthetics for

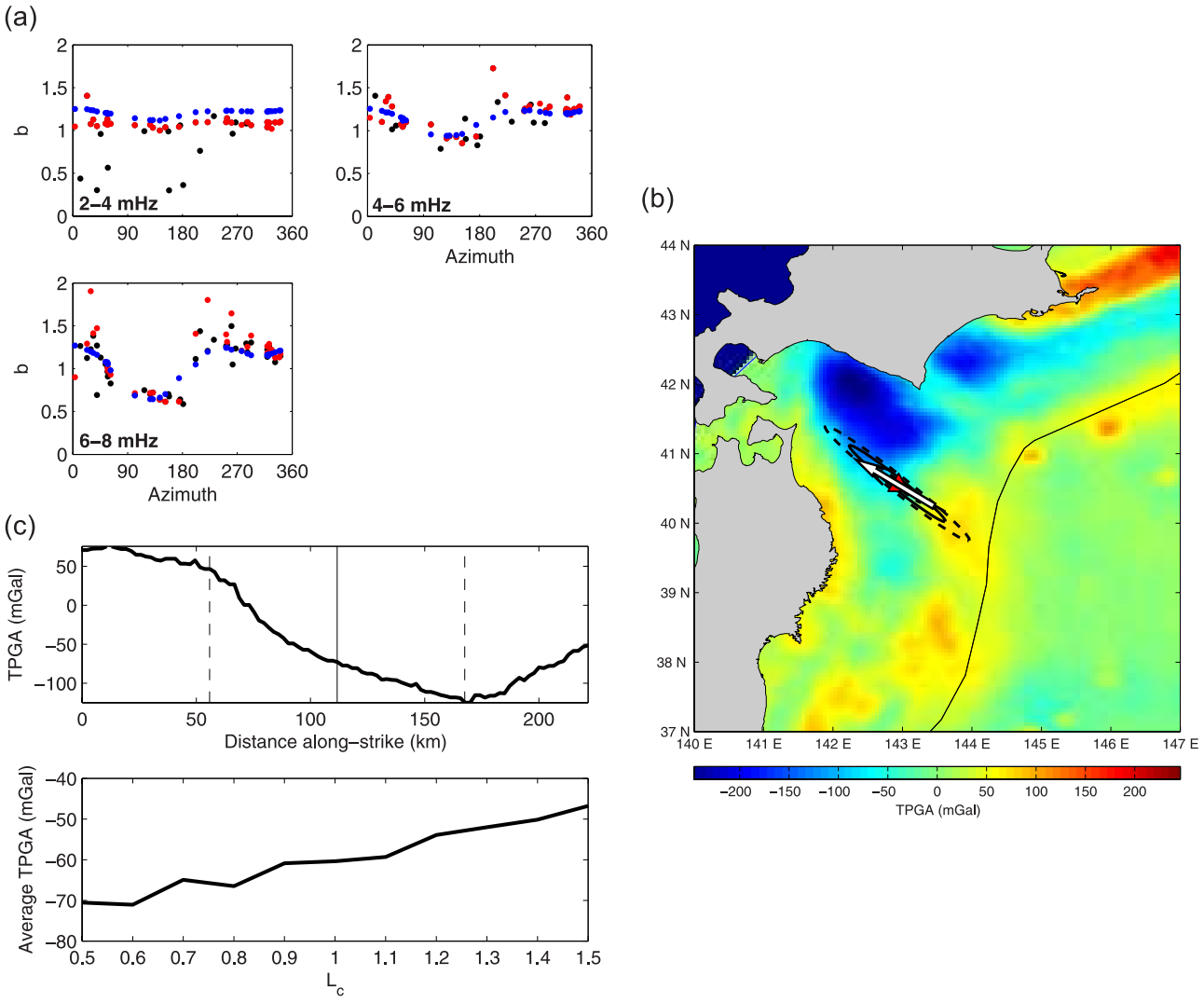

Figure B4. Measurements and results for event 19941228 in Japan made using a M_w 6.7 aftershock that occurred on 6 January 1995 as an empirical Green's function. (a) Amplitude measurements (red), fit from inversion (blue), and measurements from stations discarded in EGF due to poor SNR but retained in the original analysis (black). Note scatter in the lowest bandpass, as well as increase in amplitude with frequency due to differences in centroid depth of the EGF and the main shock. (b) See Figure 4 for symbol explanation. Compared to the original ellipse, this rupture ellipse has rotated by ~28°, although the centroid location, rupture length, and directivity are similar. (c) See Figure 4 for symbol explanation. Qualitatively, these TPGA plots changed very little from the original analysis.

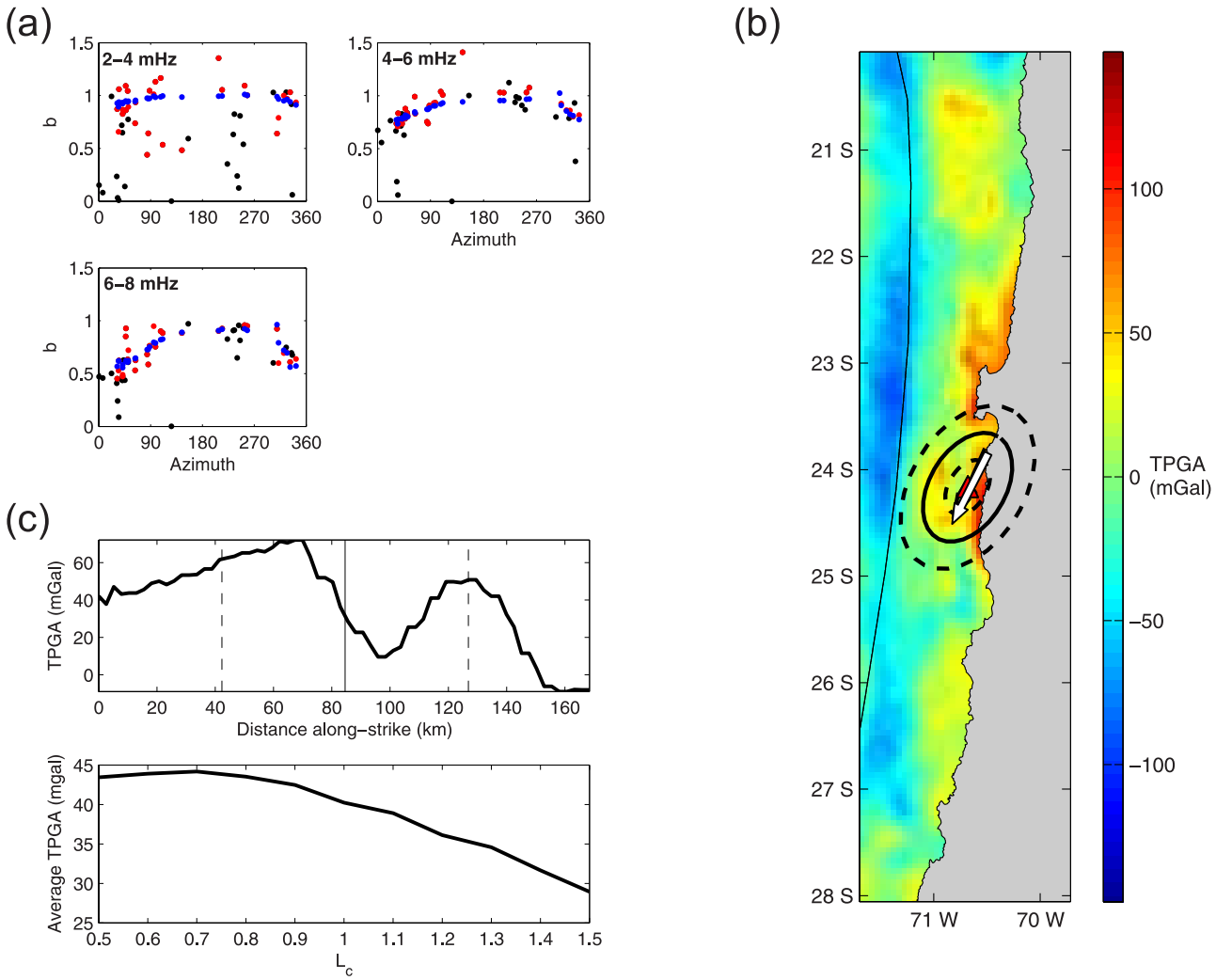

Figure B5. Measurements and results for event 19950730 in Chile using a M_w 5.9 aftershock that occurred on 3 August 1995 as an EGF. (a) See Figure B4 for symbol explanation. Note the large amount of scatter in the 2–4 mHz band. (b) See Figure 4 for symbol explanation. Compared to the TGF results, the ellipse has rotated by $\sim 14^\circ$ but remains oblique to the strike of the trench. (c) See Figure 4 for symbol explanation. Although these plots have changed slightly from the original results, the overall conclusion remains the same qualitatively.

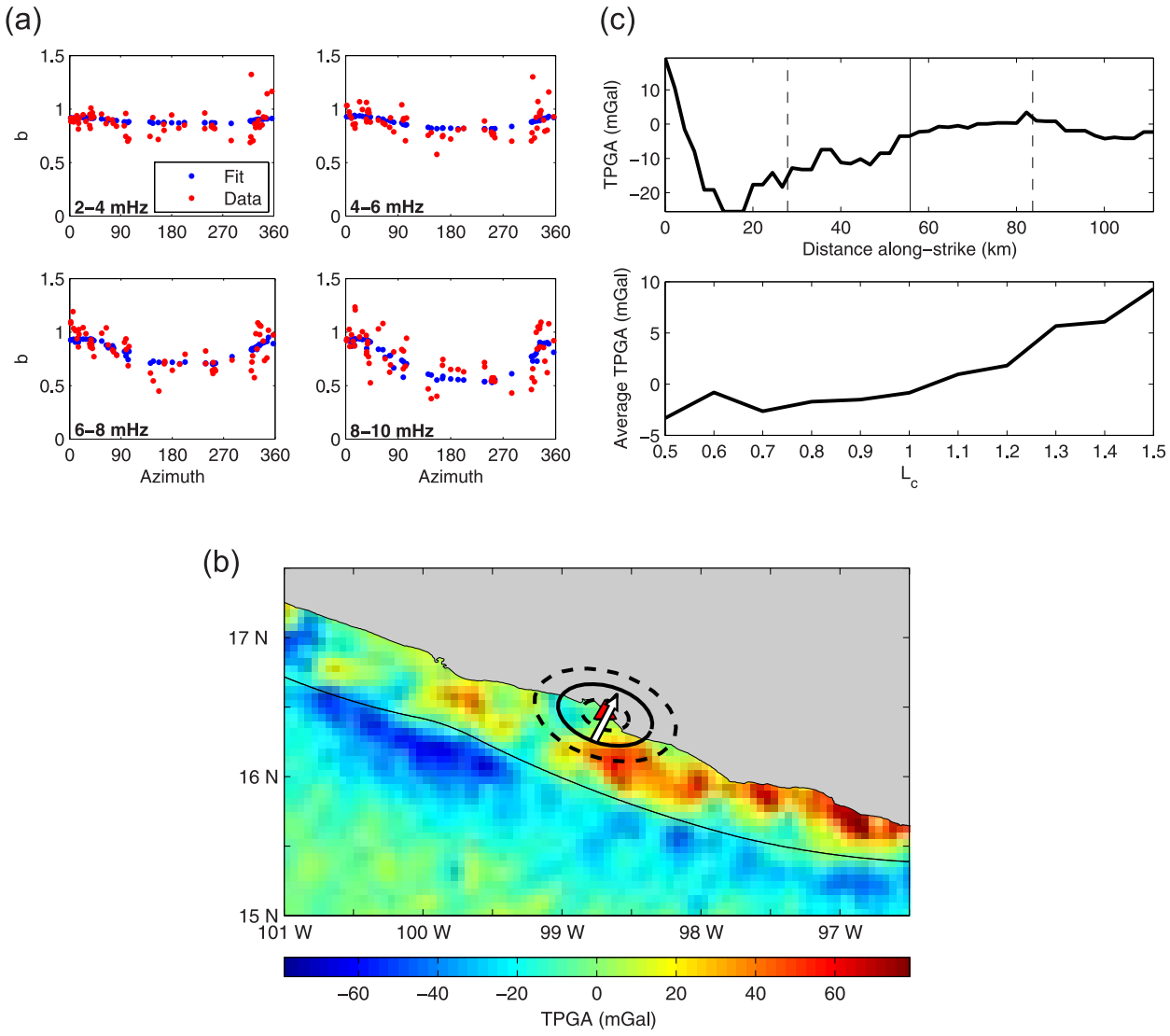

Figure B6. Measurements and results for unilateral event 19950914 in Mexico. See Figure 4 for symbol explanation.

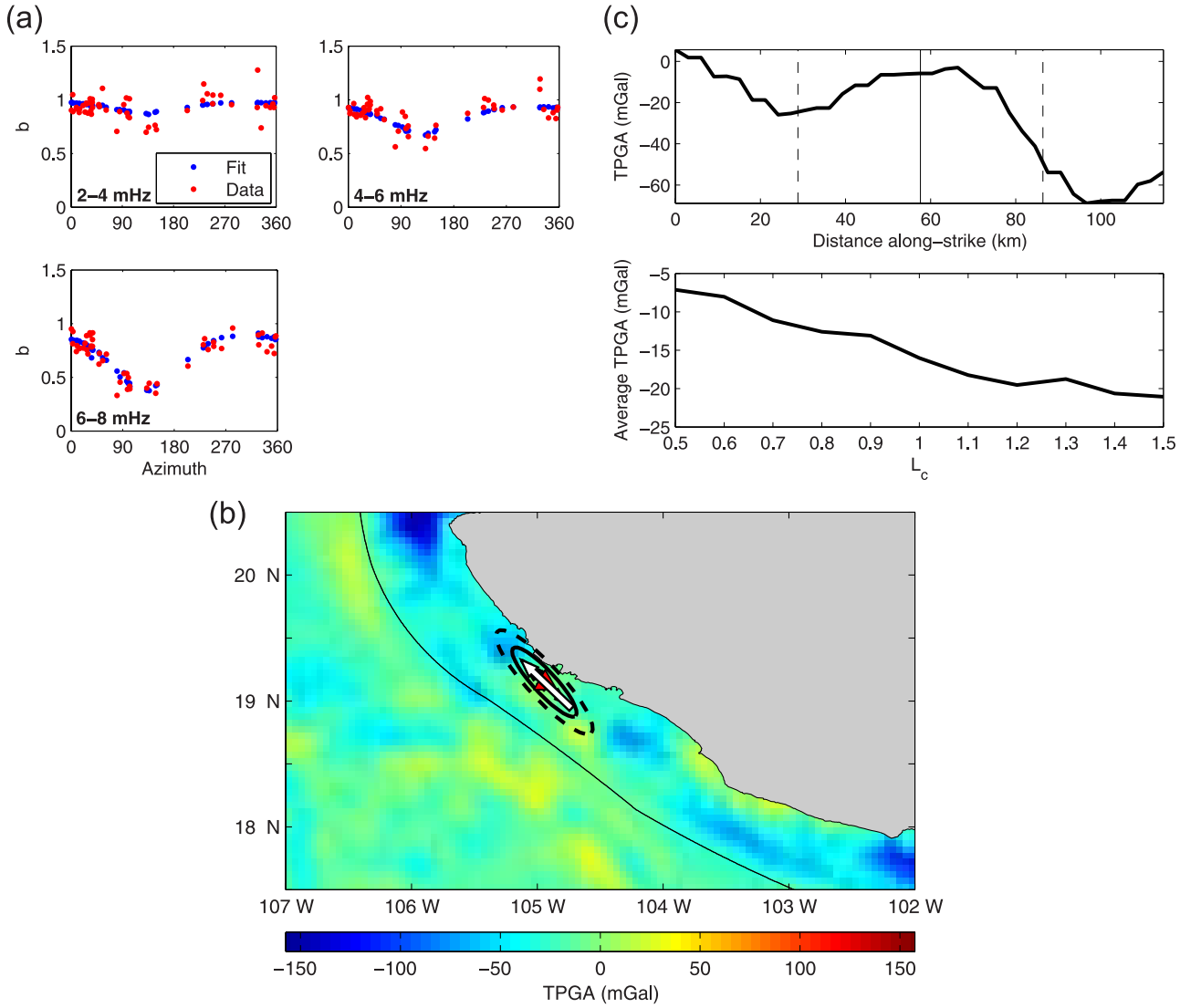

Figure B7. Measurements and results for unilateral event 19951009 in Mexico. See Figure 4 for symbol explanation.

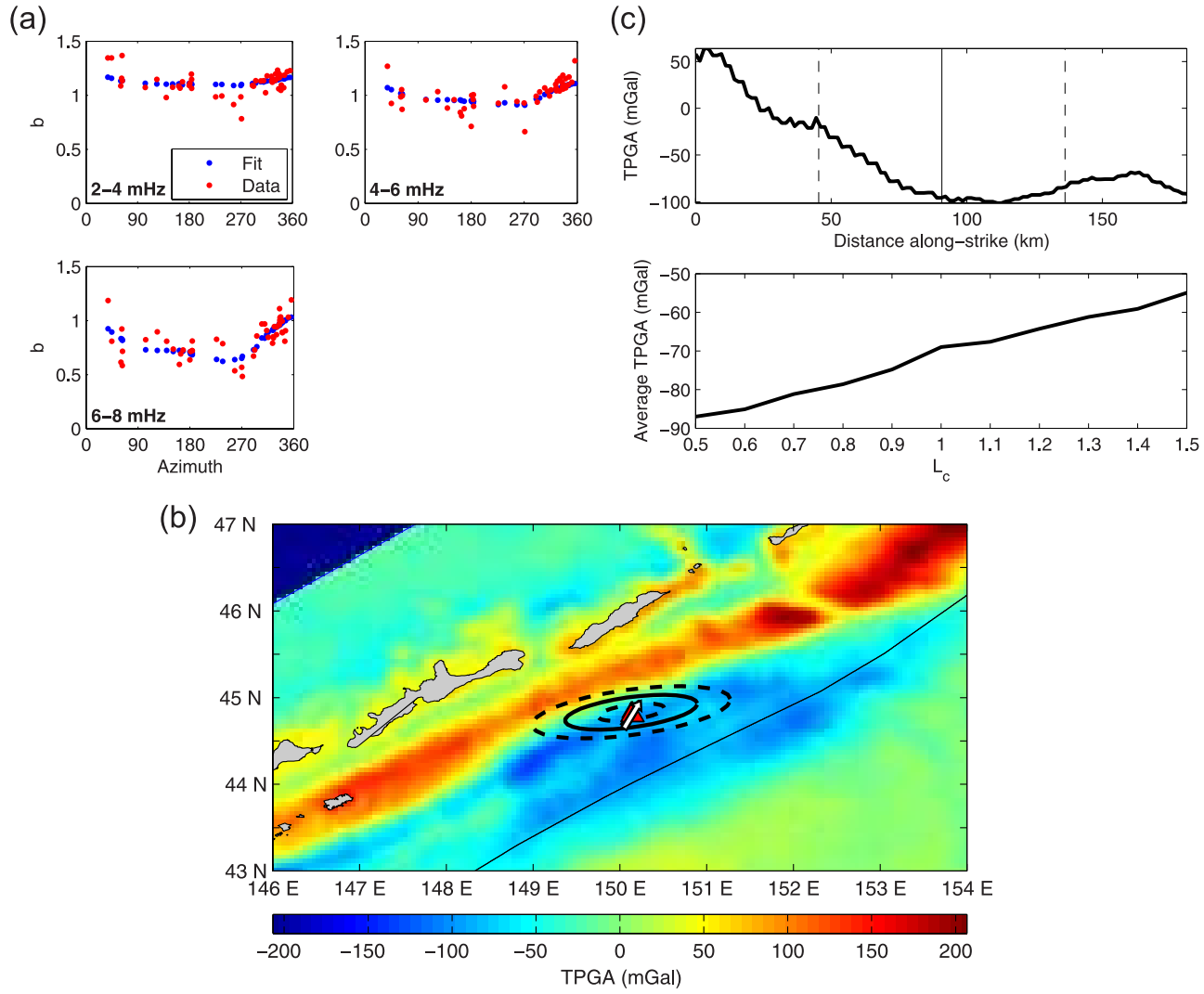

Figure B8. Measurements and results for bilateral event 19951203 in the Kurile Islands. See Figure 4 for symbol explanation.

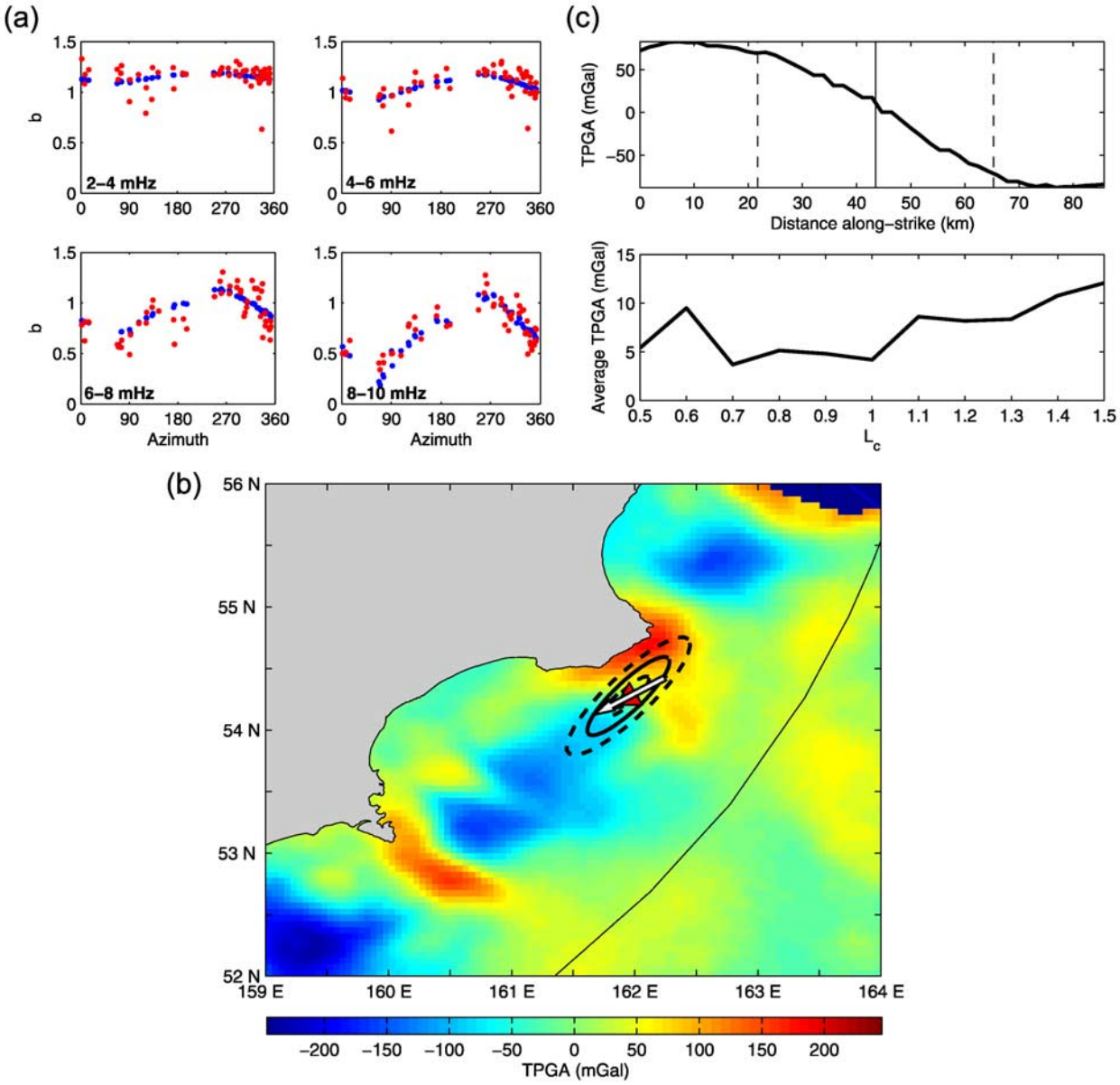

Figure B9. Measurements and results for unilateral event 19971205 in Kamchatka. See Figure 4 for symbol explanation.

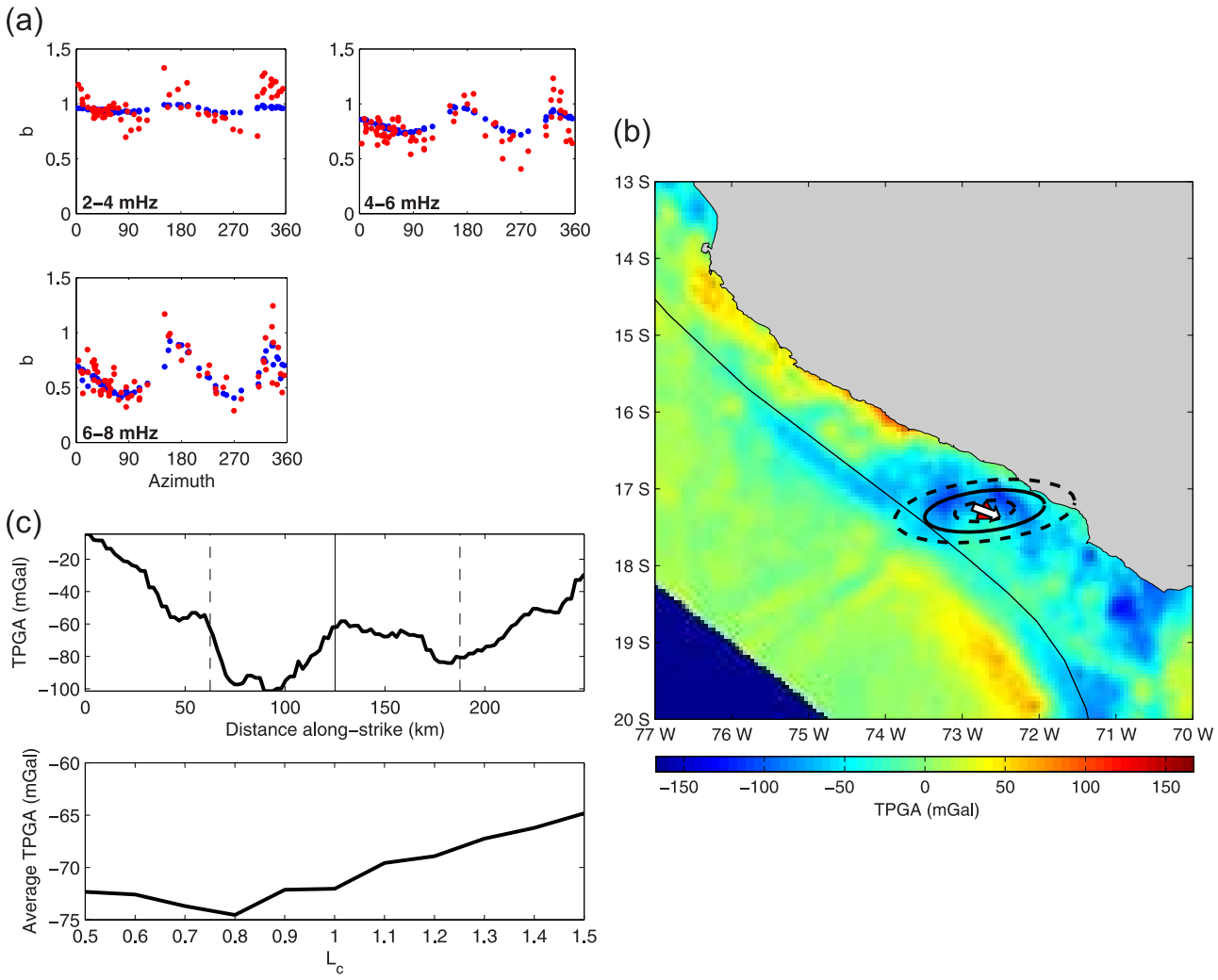

Figure B10. Measurements and results for bilateral event 20010623 in Peru. See Figure 4 for symbol explanation.

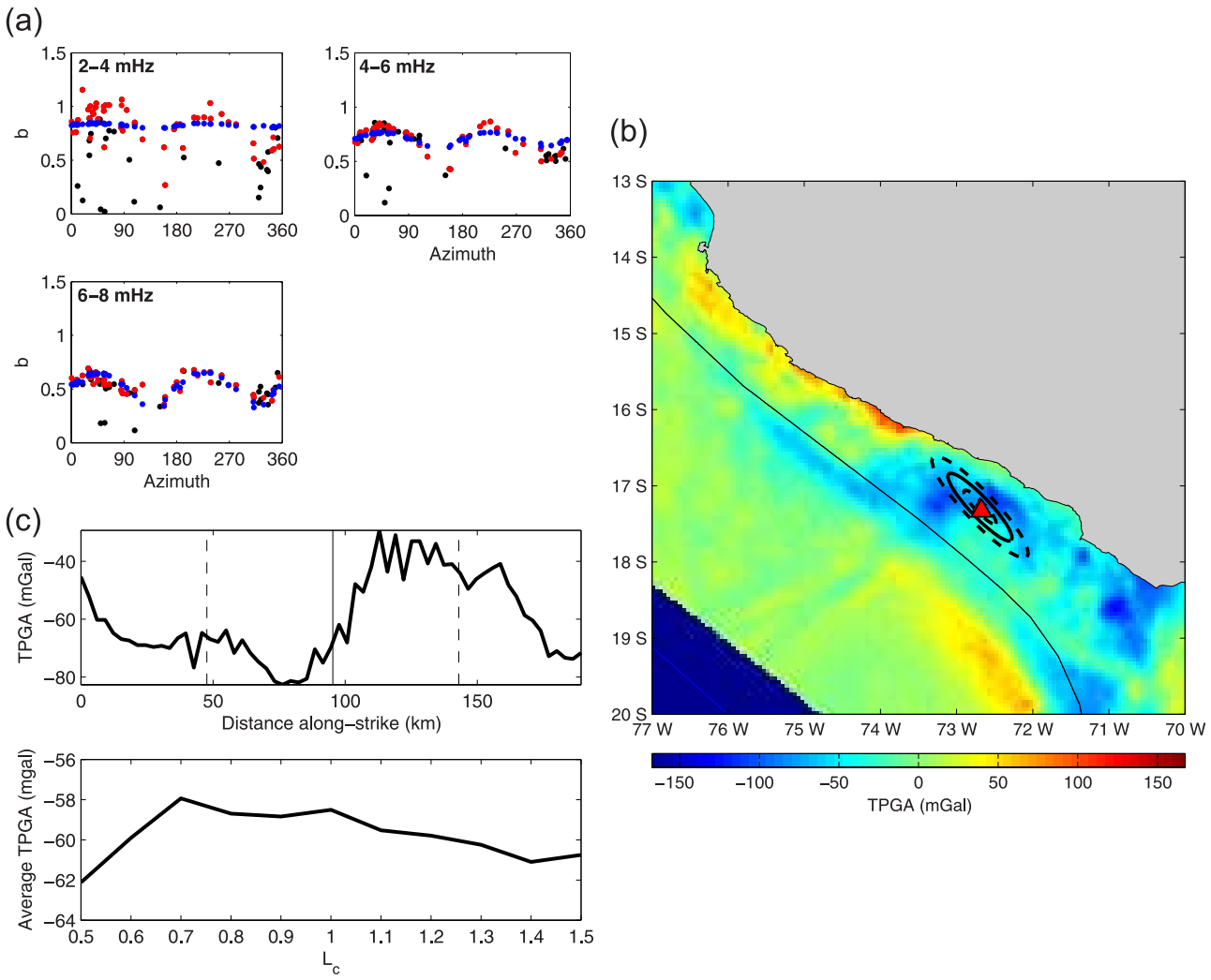

Figure B11. Measurements and results for event 20010623 in Peru, using a M_w 6.7 aftershock that occurred on 26 June 2001 as an EGF. (a) See Figure B4 for symbol explanation. Again, a large amount of scatter appears in the lowest frequency band. (b) See Figure 4 for symbol explanation. Compared to the TGF results, the ellipse has rotated by $\sim 54^{\circ}$; the orientation of the ellipse for this event is not well constrained, although the centroid location is. The directivity ratio remains very low. (c) See Figure 4 for symbol explanation. The rotation of the ellipse has caused these plots to change significantly.

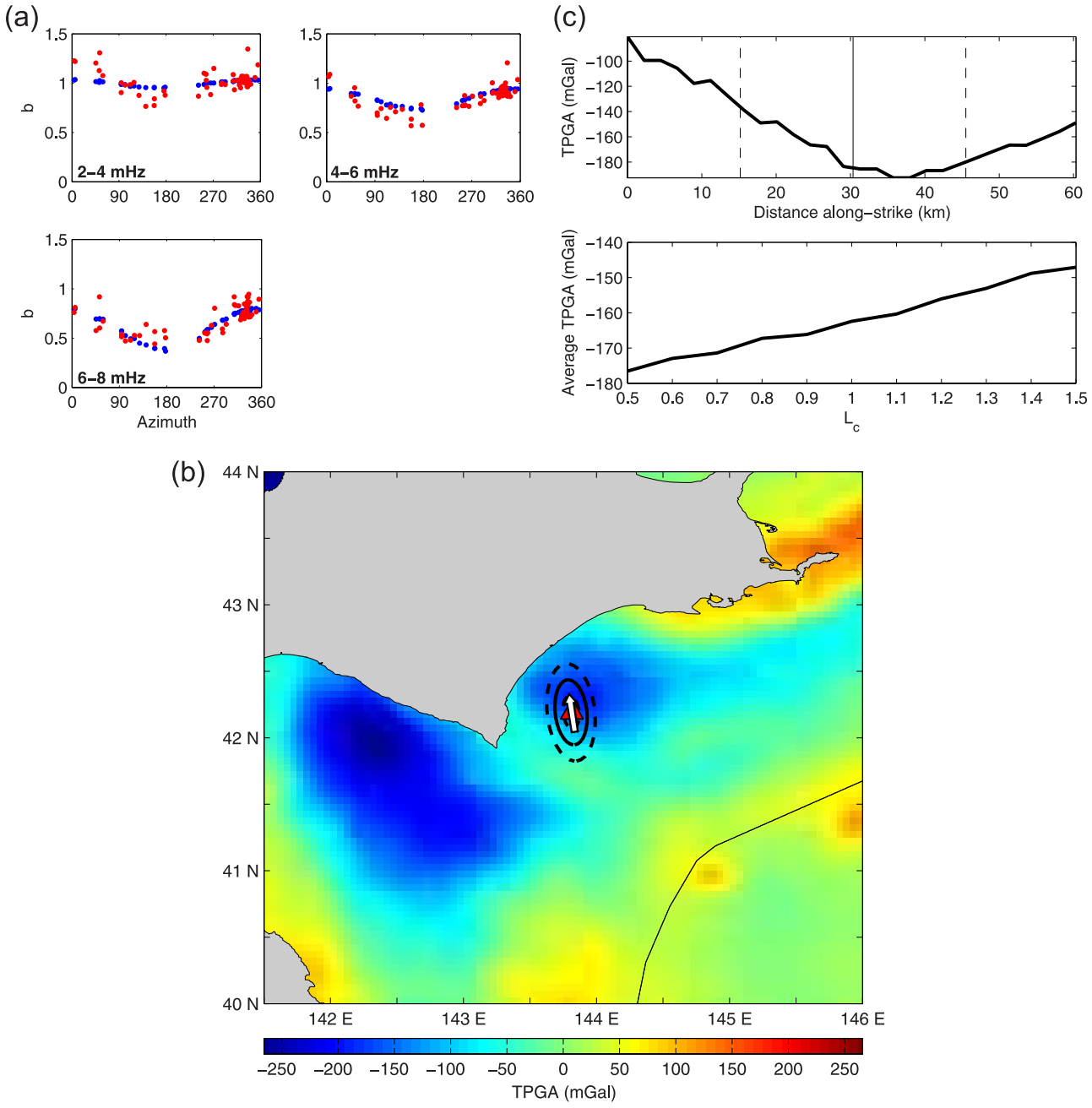

Figure B12. Measurements and results for unilateral event 20030925 in Japan. See Figure 4 for symbol explanation.

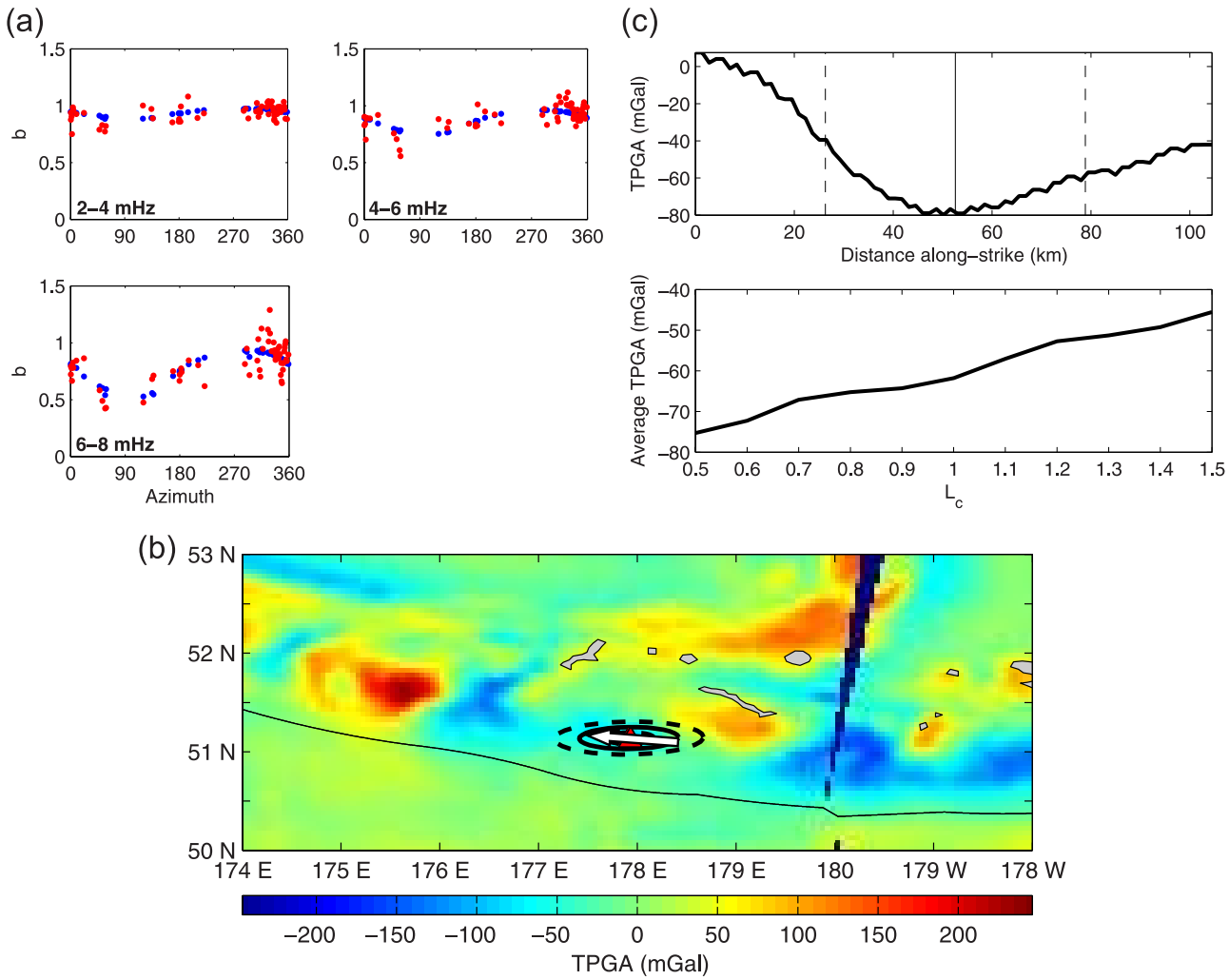

Figure B13. Measurements and results for unilateral event 20031117 in the Rat Islands. See Figure 4 for symbol explanation.

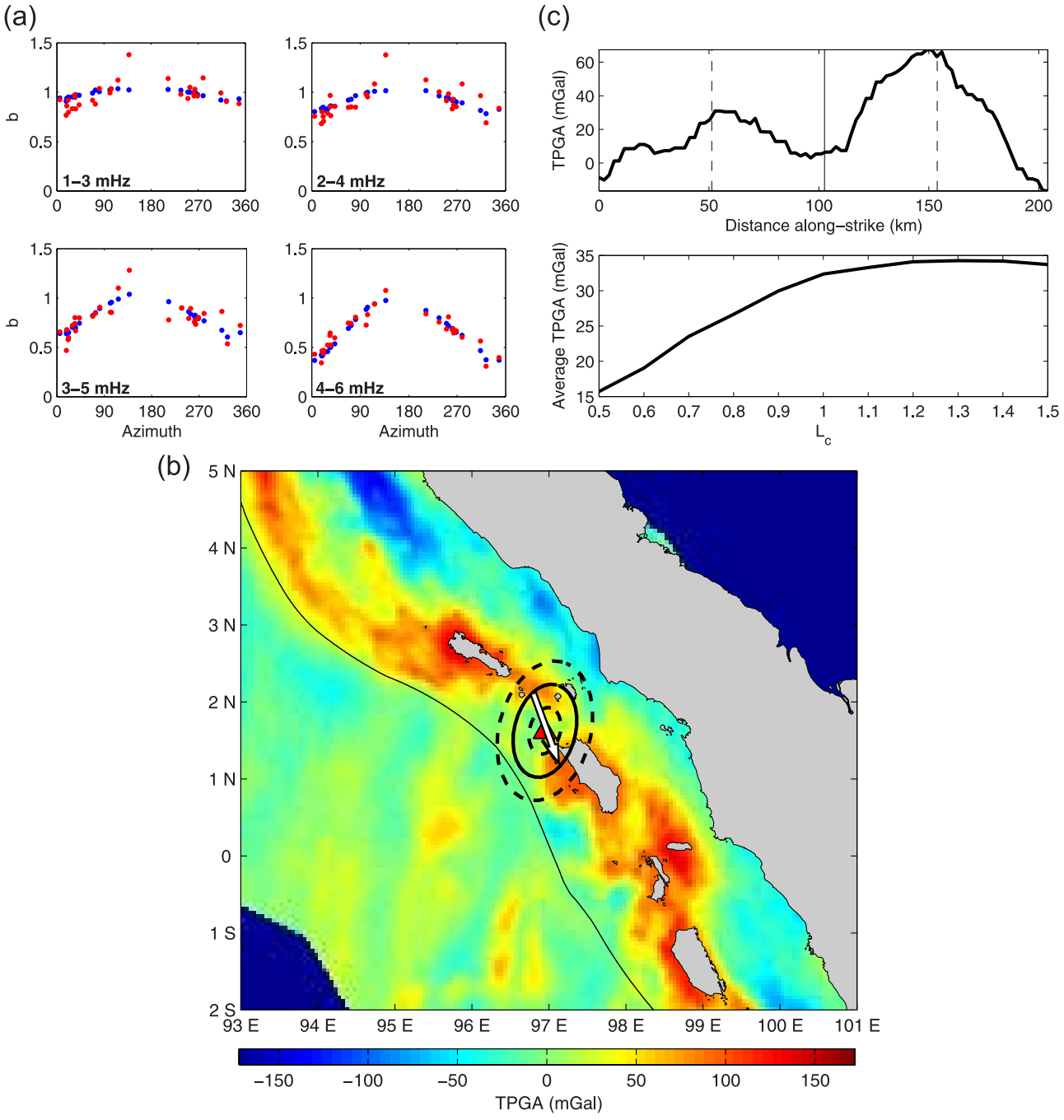

Figure B14. Measurements and results for unilateral event 20050328 in Sumatra. See Figure 4 for symbol explanation.

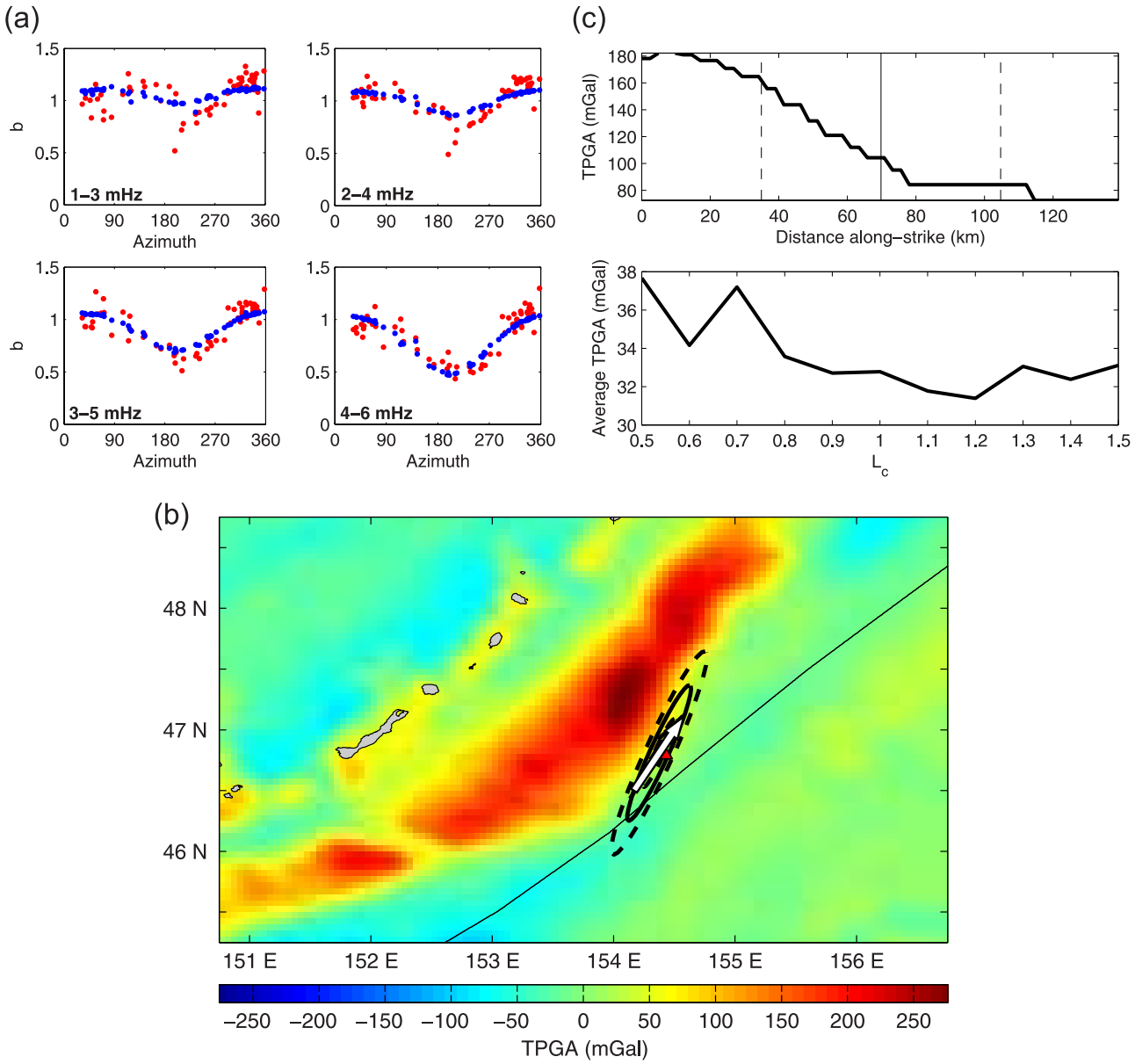

Figure B15. Measurements and results for unilateral event 20061115 in the Kurile Islands. See Figure 4 for symbol explanation.

complete station sets. Significant differences in the measurements occur at northerly azimuths in the highest frequency band. These differences alter the results of the inversion. An inversion with the 1-D synthetics resulted in a rupture length of 51 km. Using the 3-D synthetics in the inversion resulted in a rupture length of 92 km. Therefore, because the improvement in propagation modeling is significant enough to affect the inversion results, we use 3-D synthetics for the amplitude measurements.

Appendix B: Results for Additional Events

[42] This section contains the results for each event in our data set (Figures B1–B15; see Table 1 for list of events). For each event, we show Rayleigh wave measurements, estimated rupture area plotted on a TPGA map, and TPGA profiles. For three events (19941228, 19950730, and 20010623), the results using measurements made with empirical Green's functions as described in section 3.4 are also shown (Figures B4, B5, and B11, respectively). These results can be directly compared with those obtained by using point source synthetics (theoretical Green's functions) as our analysis does (Figures B3, 7, and B10).

[43] **Acknowledgments.** We thank Mark Simons for help with the TPGA maps, Martin Mai for help with the Tottori slip model, and two anonymous reviewers for their helpful comments. Seismic data for all events were obtained from the IRIS, GEOFON, GEOSCOPE, MEDNET, and China Digital networks through the IRIS Data Management Center. Centroid moment tensor solutions were obtained from the Global CMT catalog. Some figures were prepared using the Generic Mapping Tools software freely distributed by *Wessel and Smith* [1998]. A. Llenos was supported by a National Defense Science and Engineering Graduate fellowship.

References

Abercrombie, R. E., M. Antolik, K. Felzer, and G. Ekstrom (2001), The 1994 Java tsunami earthquake: Slip over a subducting seamount, *J. Geophys. Res.*, *106*, 6595–6607.

Ammon, C. J., H. Kanamori, T. Lay, and A. A. Velasco (2006), The 17 July 2006 Java tsunami earthquake, *Geophys. Res. Lett.*, *33*, L24308, doi:10.1029/2006GL028005.

Backus, G. E. (1977a), Interpreting the seismic glut moments of total degree two or less, *Geophys. J. R. Astron. Soc.*, *51*, 1–25.

Backus, G. E. (1977b), Seismic sources with observable glut moments of spatial degree two, *Geophys. J. R. Astr. Soc.*, *51*, 27–45.

Backus, G., and M. Mulcahy (1976a), Moment tensors and other phenomenological descriptions of seismic sources–I. Continuous displacements, *Geophys. J. R. Astron. Soc.*, *46*, 341–361.

Backus, G., and M. Mulcahy (1976b), Moment tensors and other phenomenological descriptions of seismic sources–II. Discontinuous displacements, *Geophys. J. R. Astron. Soc.*, *47*, 301–329.

Bassin, C., G. Laske, and G. Masters (2000), The current limits of resolution for surface wave tomography in North America, *Eos Trans. AGU*, *81*(48), Fall Meet. Suppl., Abstract S12A-03.

Bevington, P. R., and D. K. Robinson (1992), *Data Reduction and Error Analysis for the Physical Sciences*, 2nd ed., 328 pp., McGraw-Hill, New York.

Byrne, D. E., D. M. Davis, and L. R. Sykes (1988), Loci and maximum size of thrust earthquakes and the mechanics of the shallow region of subduction zones, *Tectonics*, *7*, 833–857.

Carlo, D. L., T. Lay, C. J. Ammon, and J. Zhang (1999), Rupture process of the 1995 Antofagasta subduction earthquake (M_w = 8.1), *Pure Appl. Geophys.*, *154*, 677–709.

Cloos, M. (1992), Thrust-type subduction-zone earthquakes and seamount asperities: A physical model for seismic rupture, *Geology*, *20*, 601–604.

Dalguer, L. A., K. Irikura, W. Zhang, and J. D. Riera (2002), Distribution of Dynamic and Static Stress Changes during 2000 Tottori (Japan) Earthquake: Brief Interpretation of the Earthquake Sequences; Foreshocks, Mainshock and Aftershocks, *Geophys. Res. Lett.*, *29*(16), 1758, doi:10.1029/2001GL014333.

Das, S., and B. V. Kostrov (1997), Determination of the polynomial moments of the seismic moment rate density distributions with positivity constraints, *Geophys. J. Int.*, *131*, 115–126.

Delouis, B., et al. (1997), The M_w = 8.0 Antofagasta (northern Chile) earthquake of 30 July 1995: A precursor to the end of the large 1877 gap, *Bull. Seismol. Soc. Am.*, *87*, 427–445.

Dziewonski, A. M., and D. L. Anderson (1981), Preliminary reference Earth model, *Phys. Earth Planet. Inter.*, *25*, 297–356.

Efron, B., and C. Stein (1981), The jackknife estimate of variance, *Ann. Stat.*, *9*, 586–596.

Ekstrom, G., J. Tromp, and E. W. F. Larson (1997), Measurements and global models of surface wave propagation, *J. Geophys. Res.*, *102*, 8137–8157.

Fuller, C. W., S. D. Willet, and M. T. Brandon (2006), Formation of forearc basins and their influence on subduction zone earthquakes, *Geology*, *34*, 65–68.

Fujii, Y., and K. Satake (2006), Source of the July 2006 West Java tsunami estimated from tide gauge records, *Geophys. Res. Lett.*, *33*, L24317, doi:10.1029/2006GL028049.

Guatteri, M., and P. Spudich (2000), What can strong-motion data tell us about slip-weakening fault-friction laws?, *Bull. Seismol. Soc. Am.*, *90*, 98–116.

Honda, R., S. Aoi, N. Morikawa, H. Sekiguchi, T. Kunugi, and H. Fujiwara (2004), Ground motion and rupture process of the 2003 Tokachi-oki earthquake obtained from strong motion data of K-NET and KiK-net, *Earth Planets Space*, *56*, 317–322.

Hyndman, R. D., and K. Wang (1993), Thermal constraints on the zone of major thrust earthquake failure: The Cascadia subduction zone, *J. Geophys. Res.*, *98*, 2039–2060.

Ihmlé, P. F., and J.-C. Ruegg (1997), Source tomography by simulated annealing using broad-band surface waves and geodetic data: Application to the M_w = 8.1 Chile 1995 event, *Geophys. J. Int.*, *131*, 146–158.

Iwata, T., H. Sekiguchi, Y. Matsumoto, H. Miyake, and K. Irikura (2000), Source process of the 2000 Western Tottori Prefecture earthquake and near-source strong ground motion, paper presented at the 2000 Fall Meeting, Seismol. Soc. of Jpn., Hokkaido, Japan.

Kelleher, J., and W. McCann (1976), Buoyant zones, great earthquakes, and unstable boundaries of subduction, *J. Geophys. Res.*, *81*, 4885–4896.

Kodaira, S., N. Takahashi, A. Nakanishi, S. Miura, and Y. Kaneda (2000), Subducted seamount imaged in the rupture zone of the 1946 Nankaido earthquake, *Science*, *289*, 104–106.

Kodaira, S., E. Kurashimo, J.-O. Park, N. Takahashi, A. Nakanishi, S. Miura, T. Iwasaki, N. Hirata, K. Ito, and Y. Kaneda (2002), Structural factors controlling the rupture progress of a megathrust earthquake at the Nankai trough seismogenic zone, *Geophys. J. Int.*, *149*, 815–835.

Koketsu, K., K. Hikima, S. Miyazaki, and S. Ide (2004), Joint inversion of strong motion and geodetic data for the source process of the 2003 Tokachi-oki, Hokkaido, earthquake, *Earth Planets Space*, *56*, 329–334.

Komatitsch, D., and J. Tromp (1999), Introduction to the spectral element method for three-dimensional seismic wave propagation, *Geophys. J. Int.*, *139*, 806–822.

Lay, T., and S. L. Bilek (2007), Anomalous earthquake ruptures at shallow depths on subduction zone megathrusts, in *The Seismogenic Zone of Subduction Thrust Faults*, edited by T. Dixon and C. Moore, Columbia Univ. Press, New York, in press.

Lay, T., and H. Kanamori (1981), An asperity model of great earthquake sequences, in *Earthquake Prediction: An International Review*, *Maurice Ewing Ser.*, vol. 4, edited by D. Simpson and P. Richards, pp. 579–592, AGU, Washington, D. C.

Lay, T., H. Kanamori, and L. Ruff (1982), The asperity model and the nature of large subduction zone earthquakes, *Earthquake Predict. Res.*, *1*, 3–71.

Marone, C. (1998), Laboratory-derived friction laws and their application to seismic faulting, *Annu. Rev. Earth Planet. Sci.*, *26*, 643–696.

McCaffrey, R. (1993), On the role of the upper plate in great subduction zone earthquakes, *J. Geophys. Res.*, *98*, 11,953–11,966.

McGuire, J. J., L. Zhao, and T. H. Jordan (2001), Teleseismic inversion for the second-degree moments of earthquake space-time distributions, *Geophys. J. Int.*, *145*, 661–678.

McGuire, J. J., L. Zhao, and T. H. Jordan (2002), Predominance of unilateral rupture for a global catalog of large earthquakes, *Bull. Seismol. Soc. Am.*, *92*, 3309–3317.

Miyazaki, S., K. M. Larson, K. Choi, K. Hikima, K. Koketsu, P. Bodin, J. Haase, G. Emore, and A. Yamagiwa (2004a), Modeling the rupture process of the 2003 September 25 Tokachi-Oki (Hokkaido) earthquake using 1–Hz GPS data, *Geophys. Res. Lett.*, *31*, L21603, doi:10.1029/2004GL021457.

Miyazaki, S., P. Segall, J. Fukuda, and T. Kato (2004b), Space time distribution of afterslip following the 2003 Tokachi-oki earthquake: Impli-

cations for variations in fault zone frictional properties, *Geophys. Res. Lett.*, *31*, L06623, doi:10.1029/2003GL019410.
Mogi, K. (1969), Relationship between the occurrence of great earthquakes and tectonic structures, *Bull. Earthquake Res. Inst. Univ. Tokyo*, *47*, 429–451.
Nishimura, T., T. Hirasawa, S. Miyazaki, T. Sagiya, T. Tada, S. Miura, and K. Tanaka (2004), Temporal change of interplate coupling in northeastern Japan during 1995–2002 estimated from continuous GPS observations, *Geophys. J. Int.*, *157*, 901–916.
Oleskevich, D. A., R. D. Hyndman, and K. Wang (1999), The updip and downdip limits to great subduction earthquakes: Thermal and structural models of Cascadia, south Alaska, SW Japan, and Chile, *J. Geophys. Res.*, *104*, 14,965–14,991.
Pacheco, J. F., L. R. Sykes, and C. H. Scholz (1993), Nature of seismic coupling along simple plate boundaries of the subduction type, *J. Geophys. Res.*, *98*, 14,133–14,159.
Polet, J., and H. Kanamori (2000), Shallow subduction zone earthquakes and their tsunamigenic potential, *Geophys. J. Int.*, *142*, 684–702.
Pritchard, M. E., C. Ji, and M. Simons (2006), Distribution of slip from 11 $M_w > 6$ earthquakes in the northern Chile subduction zone, *J. Geophys. Res.*, *111*, B10302, doi:10.1029/2005JB004013.
Pritchard, M. E., E. O. Norabuena, C. Ji, R. Boroschek, D. Comte, M. Simons, T. H. Dixon, and P. A. Rosen (2007), Geodetic, teleseismic, and strong motion constraints on slip from recent southern Peru subduction zone earthquakes, *J. Geophys. Res.*, *112*, B03307, doi:10.1029/2006JB004294.
Ritsema, J., and H. J. van Heijst (2000), Seismic imaging of structural heterogeneity in Earth's mantle: Evidence for large-scale mantle flow, *Sci. Progr.*, *83*, 243–259.
Ruff, L., and H. Kanamori (1980), Seismicity and the subduction process, *Phys. Earth Planet. Inter.*, *23*, 240–252.
Sandwell, D. T., and W. H. F. Smith (1997), Marine gravity anomaly from Geosat and ERS 1 satellite altimetry, *J. Geophys. Res.*, *102*, 10,039–10,054.
Scholz, C. H. (2002), *The Mechanics of Earthquakes and Faulting*, 2nd ed., 471 pp., Cambridge Univ. Press, New York.
Scholz, C. H., and J. Campos (1995), On the mechanism of seismic decoupling and back arc spreading at subduction zones, *J. Geophys. Res.*, *100*, 22,103–22,115.
Shaw, B. E. (2000), The edges of large earthquakes and the epicenters of future earthquakes: Stress-induced correlations in elastodynamic fault models, *Pure Appl. Geophys.*, *157*, 2149–2164.
Silver, P. (1983), Retrieval of source-extent parameters and the interpretation of corner frequency, *Bull. Seismol. Soc. Am.*, *73*, 1499–1511.
Silver, P. G., and T. H. Jordan (1983), Total-moment spectra of fourteen large earthquakes, *J. Geophys. Res.*, *88*, 3273–3293.
Song, T. A., and M. Simons (2003), Large trench-parallel gravity variations predict seismogenic behavior in subduction zones, *Science*, *301*, 630–633.
Thatcher, W. (1989), Earthquake recurrence and risk assessment in circum-Pacific seismic gaps, *Nature*, *341*, 432–434.
Tichelaar, B. W., and L. J. Ruff (1993), Depth of seismic coupling along subduction zones, *J. Geophys. Res.*, *98*, 2017–2037.
Tukey, J. W. (1984), *The Collected Works of John W. Tukey*, vol. 4, edited by L. Jones, Wadsworth and Brooks/Cole, Monterey, Calif.
Vandenberghe, L., and S. Boyd (1996), Semidefinite programming, *SIAM Rev.*, *38*, 49–95.
von Huene, R., and C. R. Ranero (2003), Subduction erosion and basal friction along the sediment-starved convergent margin off Antofagasta, Chile, *J. Geophys. Res.*, *108*(B2), 2079, doi:10.1029/2001JB001569.
Wang, K., and Y. Hu (2006), Accretionary prisms in subduction earthquake cycles: The theory of dynamic Coulomb wedge, *J. Geophys. Res.*, *111*, B06410, doi:10.1029/2005JB004094.
Wells, R. E., R. J. Blakely, Y. Sugiyama, D. W. Scholl, and P. A. Dinterman (2003), Basin-centered asperities in great subduction zone earthquakes: A link between slip, subsidence, and subduction erosion?, *J. Geophys. Res.*, *108*(B10), 2507, doi:10.1029/2002JB002072.
Wessel, P., and W. H. F. Smith (1998), New, improved version of Generic Mapping Tools released, *Eos Trans. AGU*, *79*(47), 579.
Wibberley, C. A., and T. Shimamoto (2005), Earthquake slip weakening and asperities explained by thermal pressurization, *Nature*, *436*, doi:10.1038/nature03901.
Yagi, Y. (2004), Source rupture process of the 2003 Tokachi-oki earthquake determined by joint inversion of teleseismic body wave and strong ground motion data, *Earth Planets Space*, *56*, 311–316.
Yagi, Y., T. Mikumo, J. Pacheco, and G. Reyes (2004), Source rupture process of the Tecoman, Colima, Mexico earthquake of 22 January 2003, determined by joint inversion of teleseismic body-wave and near-source data, *Bull. Seismol. Soc. Am.*, *94*, 1795–1807.
Yamanaka, Y., and M. Kikuchi (2003), Source process of the recurrent Tokachi-oki earthquake on September 26, 2003, inferred from teleseismic body waves, *Earth Planets Space*, *55*, 21–24.
Yamanaka, Y., and M. Kikuchi (2004), Asperity map along the subduction zone in northeastern Japan inferred from regional seismic data, *J. Geophys. Res.*, *109*, B07307, doi:10.1029/2003JB002683.

A. L. Llenos, MIT/WHOI Joint Program, 77 Massachusetts Avenue, 54-511, Cambridge, MA 02139, USA. (allenos@mit.edu)
J. J. McGuire, Department of Geology and Geophysics, Woods Hole Oceanographic Institution, MS 24, Woods Hole, MA 02543, USA.